

**Measurements of Energetic Electron Distributions
in UV and IR Laser Plasmas**

by

Robert Lyon Keck

**Submitted in Partial Fulfillment
of the
Requirements for the Degree
DOCTOR OF PHILOSOPHY**

Supervised by Professor Leonard M. Goldman

**Department of Mechanical Engineering
College of Engineering and Applied Science**

**University of Rochester
Rochester, New York**

1983

Reviewed for Classification 8-17-81
(Date)

UNCLASSIFIED

**R. L. MCGUIRE, JR.
Authorized Derivative Classifier**

VITA

The author was born in Pasadena, California on May 17, 1954. He entered Brown University in 1972, and received a Bachelor of Science degree in Physics in 1976. That same year he entered the graduate program in Mechanical Engineering at the University of Rochester and was awarded a College Fellowship. He was awarded a Master of Science degree by the College of Engineering and Applied Science in 1977. Subsequent to 1977 he held an appointment as an LLE Fellow. His thesis research was supervised by Professor Leonard M. Goldman.

ACKNOWLEDGEMENTS

It is a pleasure to acknowledge the expert advice and continued interest of the author's advisor, Professor Leonard Goldman, throughout the course of this research. The author is most grateful to Dr. Wolf Seka for his enthusiasm and many helpful suggestions. He is also indebted to Drs. R. Steve Craxton, Martin Richardson and John Soures for their interest and advice.

Research of this type requires the assistance, sometimes unseen, of many people. Particular thanks are due to R. Boni, T. Boehly, B. Flaherty, Dr. S. Letzring, L. Forsley, D. Quick, W. Watson, R. Hutchinson, and R. Leary. To the many others whose names are omitted, the author is most grateful.

Finally, the author wishes to thank the entire staff of the Laboratory for Laser Energetics for making it the stimulating and pleasant place to work that it is.

This work was supported by the U.S. Department of Energy Office of Inertial Fusion under contract DE-AC08-80DP40124 and by the Laser Fusion Feasibility Project at the Laboratory for Laser Energetics which has the following sponsors: Empire State Electric Energy Research Corporation, General Electric Company, New York State Energy Research and Development Authority, Northeast Utilities Service Company, Southern California Edison Company, The Standard Oil Company, and University of Rochester. Such support does not imply endorsement of the content by any of the above parties.

ABSTRACT

Measurements have been made of the x-ray continuum produced by plasmas irradiated with 0.35 and 1.05 μm laser light over an intensity range of 5×10^{13} to 2×10^{15} W/cm^2 . From the x-ray continuum, which was measured over a range of 1.5 to 300 keV, both the temperature of and fractional energy in any supra-thermal electron distributions can be obtained. The measurements show the presence of a very high temperature (20-60 keV) electron distribution with either 0.35 or 1.05 μm irradiation. This component, which is attributed to the presence of the two-plasmon decay instability, is observed above an intensity of approximately 10^{14} W/cm^2 at 1.05 μm and contains less than 0.1% of the incident laser energy. With 0.35 μm irradiation, the intensity at which this component is observed is approximately a factor of 3 higher. At 1.05 μm , this very high temperature component appears in addition to a third, 2 to 7 keV, component attributed to resonance absorption.

TABLE OF CONTENTS

VITAE	ii
ACKNOWLEDGEMENTS	iii
ABSTRACT	iv
LIST OF TABLES	vii
LIST OF FIGURES	viii
CHAPTER	
I. INTRODUCTION	1
II. THEORY	4
A. RESONANCE ABSORPTION	4
B. $2\omega_p$ AND RAMAN INSTABILITIES	7
C. ELECTRON ENERGY LOSS	10
III. X-RAY DETECTORS	17
A. K-EDGE FILTERED DETECTORS	18
B. SILICON PIN DETECTORS	26
C. NaI SCINTILLATORS	27
D. FILTER-FLUORESCERS	28
IV. DATA REDUCTION AND ERROR ANALYSIS	32
A. SPECTRAL UNFOLDING	32
B. LEAST SQUARE REDUCTION	36
C. ERROR ANALYSIS	40
D. SOURCES OF ERROR	44
V. EXPERIMENT	48
A. GDL EXPERIMENTS	49
B. OMEGA EXPERIMENTS	63

VI.	DISCUSSION	69
	A. THE HOT SPECTRAL COMPONENT	70
	B. THE SUPER-HOT SPECTRAL COMPONENT	74
	C. CONCLUSIONS	82
APPENDICES		
A.	PMT CALIBRATION	83
B.	PIN CALIBRATION	88
C.	FLUORESCENT ESCAPE	90
D.	FILTER FOIL FLUORESCENCE	94
E.	FILTER AND DETECTOR SELECTION CONSIDERATIONS	100
F.	SCALING IN A NON-UNIFORM BEAM	105
	REFERENCES	108

LIST OF TABLES

V-1	GDL K-EDGE FILTERED DETECTOR SYSTEM PARAMETERS	53
V-2	GDL 0.35 μm EXPERIMENTS SUMMARY	60
V-3	GDL 1.05 μm EXPERIMENTS SUMMARY	62
V-4	OMEGA K-EDGE FILTERED DETECTOR SYSTEM PARAMETERS	64
V-5	OMEGA 1.05 μm EXPERIMENTS SUMMARY	67
D-1	DIRECT AND FLUORESCENT DETECTOR SIGNAL	99

LIST OF FIGURES

II-1	GEOMETRY FOR RESONANCE ABSORPTION	6
II-2	CALCULATED X-RAY SPECTRUM	14
II-3	CALCULATED X-RAY SPECTRUM	14
III-1	X-RAY CROSS SECTION FOR ZINC	19
III-2	TRANSMISSION OF ZINC FILTER	21
III-3	DETECTION EFFICIENCY OF NICKEL	21
III-4	IDEALIZED K-EDGE DETECTOR RESPONSE	22
III-5	FILTER-FLUORESCER GEOMETRY	29
IV-1	RESPONSE OF K-EDGE FILTERED DIODE	33
IV-2	MULTI-MAXWELLIAN SPECTRUM	37
IV-3	JOINT AND INDIVIDUAL CONFIDENCE REGIONS	43
IV-4	EFFECT OF ERROR IN T ON N	43
IV-5	X-RAY SPECTRUM AND DETECTOR RESPONSE	47
V-1	GDL TARGET AREA	50
V-2	GDL DIODE ARRAYS	52
V-3	PIN DIODE RESPONSE FUNCTIONS	54
V-4	GDL PMT ARRAY	56
V-5	NaI-PMT RESPONSE FUNCTIONS	57
V-6	DATA ACQUISITION CONFIGURATION	58
V-7	FITS TO GDL DATA	61
V-8	FITS TO OMEGA DATA	68
VI-1	HOT TEMPERATURE AT 1.05 μm	71
VI-2	RELATIVE HOT ELECTRON ENERGY AT 1.05 μm	73
VI-3	SUPER-HOT TEMPERATURE AT 1.05 μm	75

VI-4	SUPER-HOT TEMPERATURE AT 0.35 μm	76
VI-5	RELATIVE SUPER-HOT ENERGY AT 1.05 μm	78
VI-6	RELATIVE SUPER-HOT ENERGY AT 0.35 μm	79
VI-7	RELATIVE SUPER-HOT ENERGY AT 0.35 μm	81
A-1	PMT CALIBRATION CONFIGURATION	84
A-2	MCA OUTPUT	86
C-1	GEOMETRY FOR FLUORESCENT PHOTON ESCAPE	91
C-2	FRACTIONAL ESCAPE FROM NaI	91
D-1	GEOMETRY FOR FILTER FOIL FLUORESCENCE	95
D-2	DETECTOR SENSITIVITY TO FOIL FLUORESCENCE	98
D-3	DIRECT AND FLUORESCENT RESPONSE AT 30 keV	98
E-1	VARIATION IN RESPONSE WITH FILTER THICKNESS	101
E-2	OPTIMAL DETECTOR CONFIGURATION	101

CHAPTER I

INTRODUCTION

A problem of concern in laser fusion experiments is target preheating by fast electrons. These electrons deposit their energy throughout the target, heating the core, which makes compression difficult, and heating the tamper, causing it to explode rather than ablate, reducing the efficiency with which it compresses the core.

At the commonly used laser driver wavelengths of 1.05 and 10.6 μm , fast electrons are generated primarily by breaking of plasma waves created by resonance absorption of the driver at the critical surface. Since the critical density is proportional to $(1/\lambda)^2$, shorter wavelength drivers are desirable, as more of the driver energy can then be depleted by collisional absorption (inverse bremsstrahlung) before reaching the critical density. While suitable short wavelength lasers do not exist, 1.05 μm lasers can be efficiently frequency tripled^{1,2} to produce a 0.35 μm output wavelength. This is sufficiently short that absorption of the driver is mainly through inverse bremsstrahlung.³

Parametric instabilities occurring in the underdense

plasma may also produce fast electrons^{4,5} and the signatures of these instabilities have been observed with various wavelength drivers.⁶⁻⁸ Fast electrons produced by these instabilities have been observed in underdense plasmas in interactions with longer wavelength lasers.⁹⁻¹¹ They have also been observed in solid target interaction experiments at 1.05 μm in a short pulse high intensity regime.¹² Fast electron production by these instabilities is of considerable interest since, with resonance absorption absent, they are the leading potential source of fast electrons with short wavelength drivers.

In order to study fast electron generation under conditions of interest in laser fusion experiments, we have measured the x-ray continuum spectrum emitted from laser plasmas produced from solid targets. The continuum spectrum, produced by bremsstrahlung, provides a means of determining the mean energy (temperature) and total energy of electron distributions within the plasma. Measurements have been made on plasmas produced from planar targets with single beam 1.05 and 0.35 μm irradiation and from spherical targets with 24 beam 1.05 μm irradiation. Measurements were made over an intensity range of 5×10^{13} to 2×10^{15} W/cm^2 . 0.35 μm experiments were performed at pulse lengths of approximately 0.5 and 1 ns, while the 1.05 μm experiments were done with approximate 1 ns pulse lengths.

With either 1.05 or 0.35 μm irradiation, a very high energy (20-60 keV) electron distribution is observed. This high energy component, which we attribute to the presence of the two plasmon ($2\omega_p$) instability, is observed at 1.05 μm above an intensity of approximately 10^{14} W/cm² and appears to saturate above about 2×10^{14} W/cm². At 0.35 μm these values are approximately a factor of 3 higher. At 0.35 μm the super-hot temperature is found to scale roughly as $I^{1/3}$, while at 1.05 μm the data are inconclusive. The super-hot temperature is on the order of a factor of 2 higher at 1.05 μm than at 0.35 μm . The energy in the super-hot component is found to be less than 0.1% of the incident laser energy.

At 1.05 μm , the super-hot component appears in addition to the expected resonance absorption hot electron component. The expected $I^{1/3}$ scaling of T_H with intensity is observed and both T_H and the electron fraction E_H/E_{ABS} are consistent with previously measured values.^{13,14} This provides considerable confidence that the measurements are correct.

CHAPTER II

THEORY

The processes generally believed responsible for fast electron production have in common the production of electron plasma waves. If they are sufficiently large in amplitude, these waves can produce fast electrons either by electron trapping or wavebreaking. In this section an overview of these processes will be presented. In addition, a discussion of electron energy loss is given, since this process is crucial to interpretation of the x-ray continuum spectra.

A. RESONANCE ABSORPTION

An important effect with longer wavelength laser drivers is resonance absorption. This occurs when the laser is incident on the plasma with a component of its electric vector along the density gradient. This component then resonantly drives electron plasma oscillations at the critical surface. The plasma oscillations, which are effectively undamped, grow in amplitude until overtaking occurs and the wave breaks. This results in the production of fast elec-

trons emitted down the density gradient. It is this process which is generally believed responsible for the production of the "hot" electron component seen in experiments with longer wavelength drivers.

The geometry for resonance absorption is illustrated in figure II-1. The EM wave is incident on the plasma at non-normal incidence, with a component of its electric vector in the plane of incidence. The dispersion relation for the EM wave is:

$$\omega_0^2 = \omega_p^2 + k^2 c^2 \quad (1)$$

where $\omega_p^2 = 4\pi n_e e^2 / m_e$. Hence, the index of refraction is $n = (1 - \omega_p^2 / \omega_0^2)^{-1/2}$. This is less than 1, so the wave will refract out of the plasma as illustrated. The turning point density can be obtained by noting that $k_y = k_0 \sin\theta$ is constant, which from equation (1) gives $n_T = n_c \cos^2\theta$, where θ is the angle of incidence.

The EM wave does not vanish inside the turning point, but is evanescent. In order to maximize coupling to the critical surface, the turning point needs to be close to critical, which implies small angles of incidence. A competing effect is that $E_x \propto E_0 \sin\theta$, thus favoring large angles of incidence. The optimum angle of incidence can be determined analytically for certain fixed density profiles. However, in numerical simulations, density profile steepening is found to occur near the critical surface which

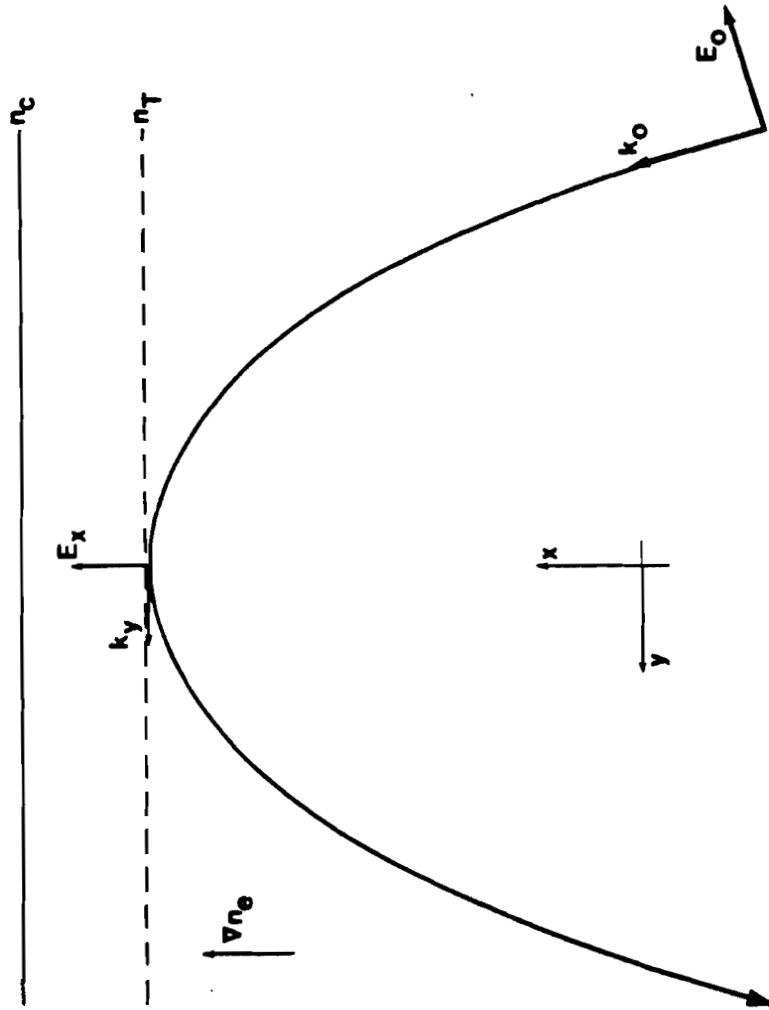


Figure II-1. Geometry for resonance absorption. An electromagnetic wave is incident on the plasma with a component of its electric vector along the density gradient.

broadens the range of angles over which coupling is effective.¹⁵

That portion of E_x which makes it to critical then resonantly drives electron plasma oscillations. These oscillations are effectively undamped, and grow in amplitude until non-linear saturations occurs, e.g. wavebreaking. The large electric fields produced accelerate electrons which enter the resonant region down the density gradient and also result in density profile steepening near critical.¹⁵⁻¹⁷

Numerical simulations^{16,17} indicate that the electrons produced through resonance absorption have an approximately Maxwellian distribution with T_H scaling approximately as $(I\lambda^2)^{1/3}$. Ref. 16 finds:

$$T_H \approx 7(I\lambda^2)^{1/3} T_C^{1/3}$$

while ref. 17 finds:

$$T_H \approx 13(I\lambda^2)^{0.39} T_C^{1/4}$$

where λ is the laser wavelength in μm , I is the laser intensity in units of 10^{15} W/cm^2 and T_C , the background plasma temperature, and T_H are in keV.

B. $2\omega_p$ AND RAMAN INSTABILITIES

The $2\omega_p$ and Raman instabilities can occur at $n_e = n_c/4$. Raman can also occur at $n_e < n_c/4$, but at $n_e = n_c/4$ it is

absolute and has a lower threshold. Both these instabilities produce electron plasma waves with very high phase velocities and thus can potentially generate very fast electrons. It is to these instabilities, in particular $2\omega_p$, that the "super hot" electron component observed in these experiments is attributed.

In $2\omega_p$, the incident EM wave decays into two electron plasma waves. From the frequency matching condition $\omega_0 = \omega_1 + \omega_2$ it will be seen that the two electron plasma waves have a frequency of approximately $\omega_0/2$. The $2\omega_p$ instability can occur when¹⁸:

$$(v_o/v_e)^2 k_0 L > 3$$

where v_o is the jitter velocity of the electrons in the pump field, v_e is the electron thermal velocity and L is the plasma density scale length. The factor 3, which appears in (2) is found in ref. 18 to depend weakly on the plasma conditions through a parameter $v_e^4/v_o^2 c^2$.

In the Raman instability, the incident EM wave decays into a plasma wave and an EM wave of lower frequency. At $n_e = n_c/4$, both the plasma wave and Raman scattered wave have a frequency of approximately $\omega_0/2$. This instability can occur when¹⁹:

$$(v_o/v_e)^{3/2} k_0 L > 1 .$$

Since both the $2\omega_p$ and Raman instabilities produce electron plasma waves, there exists the potential for fast

electron production. Whether produced by wavebreaking or trapping, the temperature of the electrons would be expected to be crudely:

$$T_{SH} \approx m_e v_\phi^2 / 2$$

where m_e is the electron mass and v_ϕ is the phase velocity of the plasma wave. The dispersion relation for the plasma wave is:

$$\omega^2 = \omega_p^2 + 3k^2 v_e^2.$$

Combining (5) with (1) and the k matching condition, $v_\phi \approx c/\sqrt{3}$ is obtained for $2\omega_p$.

Numerical simulations indicate that these instabilities generate electron distributions that are approximately Maxwellian.⁴ It is also found in ref. 4 that profile steepening occurs near $n_c/4$ which in part serves to saturate the instabilities. This is in contrast to resonance absorption where profile steepening enhances the coupling rather than limiting it. The temperature of the super hot distribution produced is found in simulations²⁰ to scale as $T_{SH} \propto (I\lambda^2)^{1/3}$. Because of its lower threshold, the $2\omega_p$ should appear before Raman. In addition, numerical simulations⁴ indicate that $2\omega_p$ probably dominates Raman at $n_e = n_c/4$.

C. ELECTRON ENERGY LOSS

The utility of the x-ray continuum measurements lies in the fact that it is possible to extract from the x-ray spectrum both the temperatures and the energy content of the electron distributions which produced the spectrum. That the slope of the x-ray continuum is proportional to the electron temperature has been known for a long time. The fact that the total energy in a fast electron distribution may also be obtained from the continuum was a result obtained by Brueckner²¹ in 1977. Because of the importance of this result to the interpretation of the measurements described in this thesis, some of the key features of Brueckner's paper will be reproduced here. Where equations given here reproduce those in ref. 21, the original equation numbers will appear in square brackets.

The radiation emitted by an electron as it slows down is given by:

$$\frac{d^2 \epsilon_{\text{rad}}}{dh\nu dx} = \frac{8}{3} \langle Z^2 \rangle n_i \frac{e^2}{4\pi c} \frac{e^2}{mc^2} \frac{1}{\epsilon} G_{\text{rad}} \quad [1](6)$$

ϵ_{rad} is the energy radiated by the electron, x is the path length, Z the ion charge, n_i the ion density, and the physics is hidden in the factor G_{rad} , a slowly varying function of ϵ , the electron energy, and $h\nu$. Then the spectrum produced by the electron in slowing down is:

$$\frac{d\epsilon_{\text{rad}}}{dh\nu} = \int \frac{d^2\epsilon_{\text{rad}}}{dh\nu dx} dx = \int_{\epsilon_0}^{h\nu} \frac{d^2\epsilon_{\text{rad}}}{dh\nu dx} \frac{dx}{d\epsilon} d\epsilon \quad (7)$$

where the upper limit in the last integral results from the fact that an electron cannot radiate at a frequency ν if its energy is less than $h\nu$.

In the absence of losses to fast ions, the electrons lose energy primarily through collisions so the factor $dx/d\epsilon$ in equation (7) will be determined by the collisional energy loss rate. This is:

$$\left(\frac{d\epsilon}{dx}\right)_{\text{coll}} = -\frac{2\pi}{\epsilon} e^4 n_{e,pl} \ln\Lambda \quad [4](8)$$

where $n_{e,pl}$ is the density of the cold electrons in which the fast electron is slowing down and $\ln\Lambda$ is the Coulomb logarithm. Using (8) in (7) we obtain:

$$\frac{d\epsilon_{\text{rad}}}{dh\nu} = \frac{4}{3\pi} \frac{e^2}{\hbar c} \frac{1}{mc^2} \int_{h\nu}^{\epsilon_0} \frac{G_{\text{rad}}(\epsilon, h\nu)}{\ln\Lambda} \frac{\langle Z^2 \rangle}{2} d\epsilon \quad [7](9)$$

where in replacing $n_{e,pl}$ with Zn_i it has been assumed that the fast electron density is small compared to the background plasma density in the regions where the electrons lose most of their energy.

Equation (9) provides the spectrum produced by a single electron. The total spectrum is obtained by integrating (9) over the distribution of fast electrons. If the electron distribution is represented as:

$$N(\epsilon_0) = N_0 \left(\frac{\epsilon_0}{\epsilon_f}\right)^n e^{-(\epsilon_0/\epsilon_f)} \frac{1}{\epsilon_f} \quad [13](10)$$

where, if $n = 1/2$ the distribution is Maxwellian, the total spectrum becomes:

$$\frac{dE}{dh\nu} = \frac{4}{3\pi} \frac{e^2}{\hbar c} \frac{1}{mc^2} \frac{\langle z^2 \rangle}{\langle z \rangle} E_{fast} I_n(h\nu) \quad [14](11)$$

where:

$$E_{fast} = \int_0^\infty N(\epsilon_0) d\epsilon_0 = N_0 (n+1)! \epsilon_f$$

and

$$I_n(h\nu) = \frac{1}{(n+1)!} \int_{h\nu}^\infty \frac{d\epsilon}{\epsilon_f} \frac{G_{rad}(\epsilon, h\nu)}{\ln \lambda} \times \int_\epsilon^\infty \left(\frac{\epsilon_0}{\epsilon_f}\right)^n e^{-(\epsilon_0/\epsilon_f)} \frac{d\epsilon_0}{\epsilon_f} \quad [15](12)$$

It is useful to express all energies in equation (12) in terms of ϵ_f . With this change $I_n(h\nu)$ becomes:

$$I_n(h\nu) = \frac{1}{(n+1)!} \int_{h\nu/\epsilon_f}^\infty \frac{G_{rad}(x, h\nu/\epsilon_f; \lambda)}{\ln \lambda \Big|_{\epsilon_f} + \ln x} \times \left(\int_x^\infty x_0^n e^{-x_0} dx_0 \right) dx \quad (13)$$

where G_{rad} may be approximated by:

$$G_{rad}(a, b; \lambda) = \frac{x_1}{x} \frac{1 - e^{-x}}{1 - e^{-x_1}} \ln \frac{x_1 + x}{x_1 - x} \quad [2]$$

$$x = \lambda/a^{1/2}$$

$$x_1 = \lambda/(a-b)^{1/2}$$

The parameter λ in equation (13) is equal to:

$$\lambda = \frac{2\pi ze^2}{h} \left(\frac{m}{2\epsilon_f}\right)^{1/2} = 0.733 z/\epsilon_f^{1/2} \quad [16]$$

In addition to the dependence of $I_n(h\nu)$ on λ , there is an additional dependence on ϵ_f because of the Coulomb logarithm. This dependence is slow, so $\ln\Lambda$ may be replaced with an average value, e.g. replace $\ln(x)$ with $\ln(1) = 0$ in equation (13).

Using equation (13), Brueckner's figures 1 and 2 can be easily reproduced, which has been done in figures II-2 and II-3. The apparent difference in appearance between figure II-3 and Brueckner's figure 2 is caused by the fact that in figure II-3, $I_n(h\nu) \ln\Lambda$ has been plotted as a function of $h\nu/\epsilon_f$ rather than of $h\nu/\bar{\epsilon}$. Note also that the curves have been plotted only for $n = 0$ and 1. The dashed lines show the extrapolations back to $h\nu/\epsilon_f = 0$ of the straight line portions of each curve.

Figures II-2 and II-3 illustrate a number of features of the predicted spectrum, $dE/dh\nu$. First, for $h\nu$ greater than about ϵ_f , the spectrum is exponential. Second, the spectrum is quite insensitive to the value of λ . Third, there is a moderate sensitivity of the spectrum to n .

In order for this model to be useful, the predicted and measured $dE/dh\nu$ must agree over some reasonable range of $h\nu$.

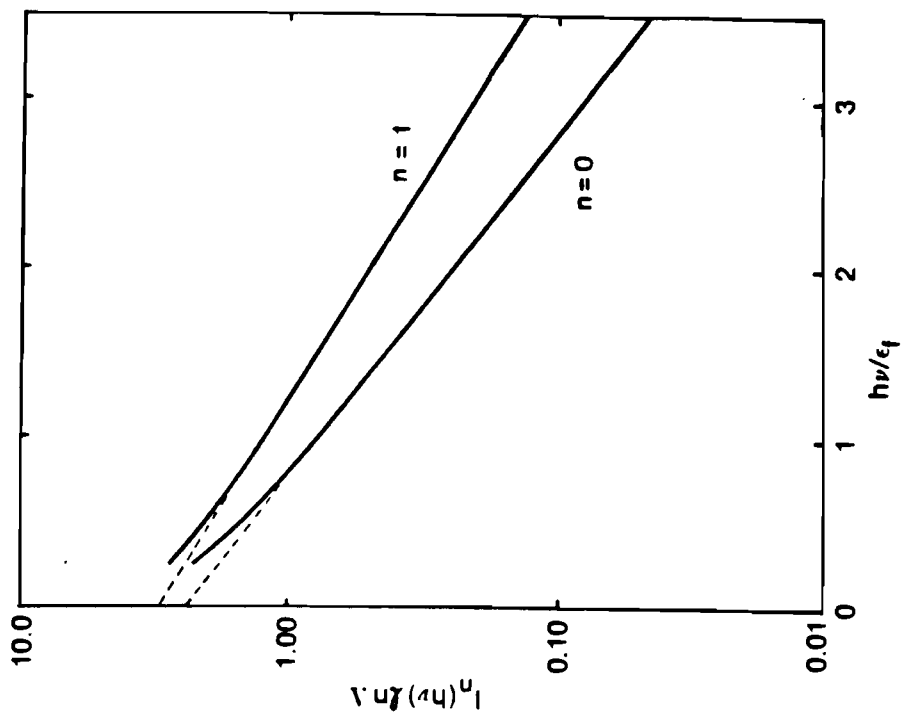


Figure II-3. Calculated x-ray spectrum for 2 values of n . For a Maxwellian distribution, $n = 1/2$.

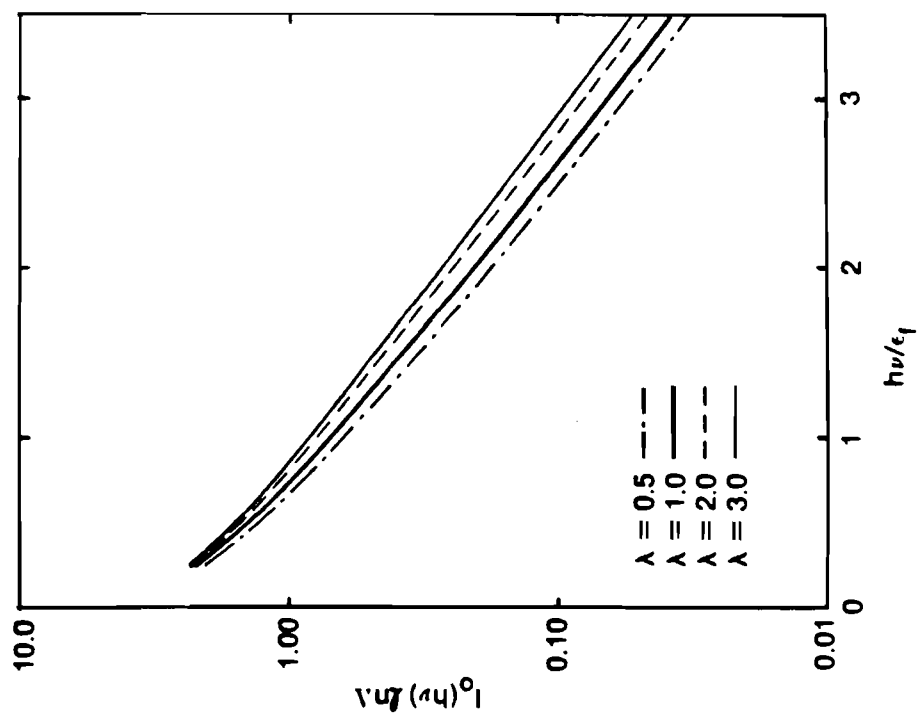


Figure II-2. Calculated x-ray spectrum for an exponential electron distribution.

As will be discussed later, the experimental data will be fit using:

$$\frac{dE}{dh\nu} = \sum_{j=1}^K N_j e^{-h\nu/T_j}$$

where the T_j are determined by $h\nu$'s greater than, or on the order of T_j . Thus, for each component, there is the required correspondence with the model. Referring to figure II-3 and measuring the slope of the straight line portion of the curves, it can be determined that T_j will differ from ϵ_f by about 10% if $n = 0$ or 1 while if $n = 0.5$, $T_j \approx \epsilon_f$.

Equation (11), may be rewritten as:

$$\left. \frac{dE}{dh\nu} \right|_{h\nu=0} = \frac{4}{3\pi} \frac{e^2}{hc} \frac{1}{mc^2} \frac{\langle Z^2 \rangle}{\langle Z \rangle} \frac{1}{\ln\Lambda} E_{\text{fast}} (I_n(0) \ln\Lambda)$$

where $I_n(0) \ln\Lambda$ is determined by extrapolating the straight line portion of the curves back to $h\nu = 0$ as shown by the dashed lines in figure II-3. So, E_j may be determined from N_j using:

$$E_j = N_j \frac{\ln\Lambda}{3.9 \times 10^{10}} \frac{\langle Z \rangle}{\langle Z^2 \rangle} \quad (14)$$

where a Maxwellian electron distribution, $n = 0.5$, has been assumed with $I_{0.5}(0) \ln\Lambda \approx 2.5$. Because n is unknown in the experiments, there is an uncertainty in $I_n(0) \ln\Lambda$. For example $I_0(0) \ln\Lambda = 1.9$ and $I_1(0) \ln\Lambda = 3$. The factor Λ is given by:

$$\Lambda = \frac{2p}{nk_D} = \frac{\sqrt{\epsilon T}}{\sqrt{n_e}} 7.6 \times 10^{13}$$

where ϵ and T are in keV and n_e in cm^{-3} .

In summary, equation (14) provides a simple means of determining the the energy in a fast electron distribution from an experimentally measured exponential x-ray spectrum. The result depends only weakly on the plasma conditions through the Coulomb logarithm. It is also fairly insensitive to the details of the actual electron distribution as long as the distribution is basically exponential.

CHAPTER III

X-RAY DETECTORS

The simplest method of determining the x-ray spectrum, $dE/dh\nu$, is to measure it at several points over the range of interest. A simple spline can then be used to approximate $dE/dh\nu$ over the measured range. To utilize this method, the x-ray detectors must have a narrow passband and their response must be uniform throughout the passband. A detector system meeting these requirements over the spectral range of interest is the filter-fluorescer.²² However, this type of detector was estimated to lack sufficient sensitivity for use on the GDL experiments. Because of this, the simpler and more sensitive K-edge detector design was used in these experiments. These detectors provide a localized, but not truly narrowband response. This requires that the spectrum be obtained from the data through a special unfolding procedure, which is described in the next chapter. The following sections cover the details of K-edge filtered detectors in general and the particular detectors used in these experiments. Also, filter-fluorescers and the difficulty in their use will be described.

It should be noted that throughout this thesis, the symbol σ and term cross section will be used to refer to what is more properly called a mass absorption coefficient. The two are related by:

$$\sigma_{MA} = \sigma N_A / (Aw 10^{24}),$$

where σ_{MA} is the x-ray mass absorption coefficient in cm^2/gm , σ is the x-ray absorption cross section in barns/atom, N_A is Avogadro's number and Aw is the atomic weight of the absorbing material. The subscript MA has been dropped throughout. When the mass absorption coefficient is used, absorber "thicknesses" are specified in gm/cm^2 .

A. K-EDGE FILTERED DETECTORS

Unlike the case in the visible, narrow band x-ray filters do not exist over the energy range of interest here (1 to 300 keV). However, the total x-ray interaction cross section for a material, for example zinc figure III-1, exhibits discontinuities or absorption edges in addition to a fall-off approximately proportional to $E^{-2.5}$. These edges, due to photoelectric absorption, occur at the energies required to remove an electron from one of the inner shells of the atom and are named for the corresponding shell (K, L, M, etc.). The cross sections for other materials exhibit the same general behavior with the location of a given edge shifting to higher energy with increasing Z .

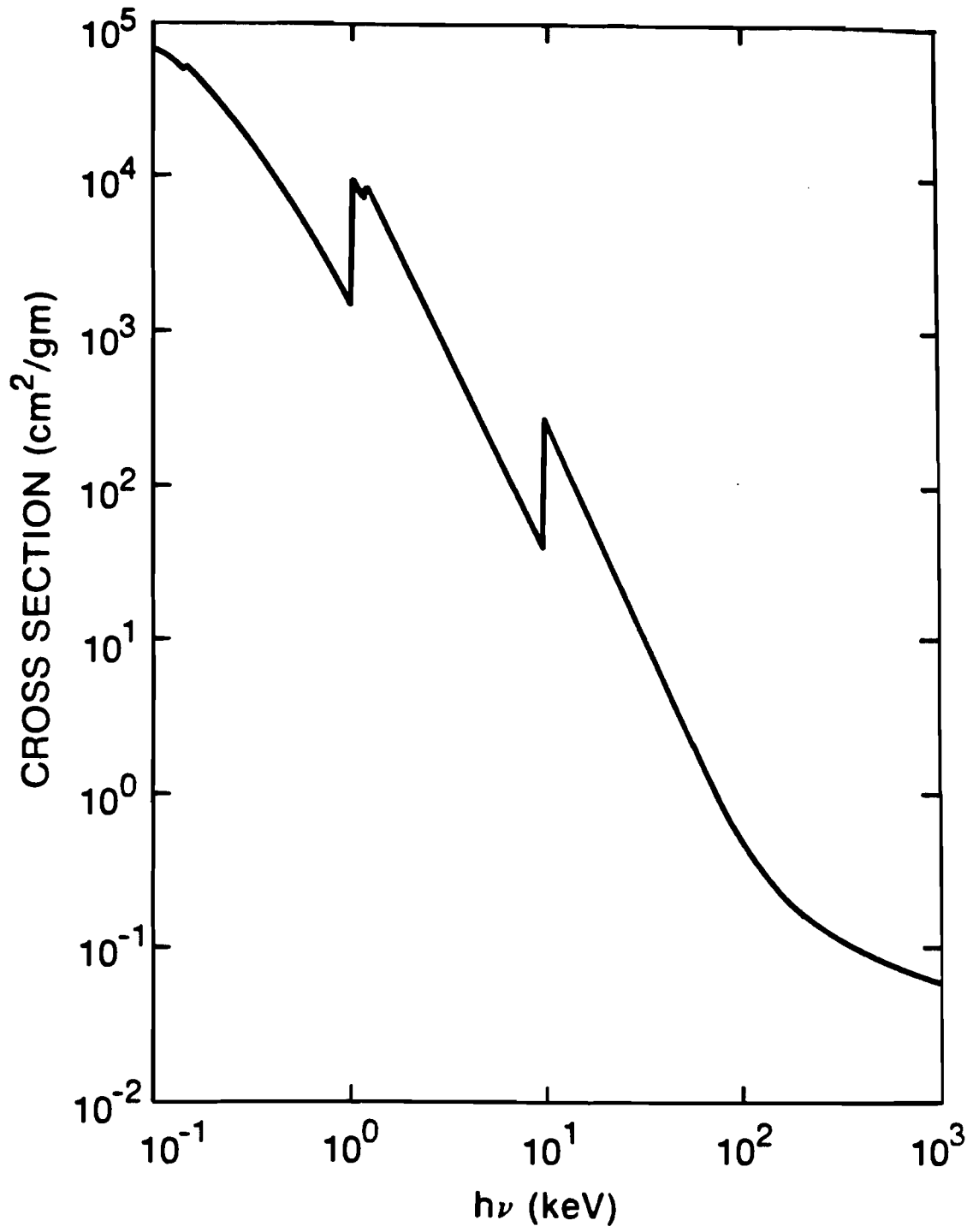


Figure III-1. Total x-ray interaction cross section of Zinc.

The transmission of a layer of material is given by $\exp(-\sigma(h\nu)X)$, where X is the thickness of the material in gm/cm^2 and $\sigma(h\nu)$ is its cross section cm^2/gm . So by choosing an appropriate thickness of material, a transmission function can be obtained which exhibits a local maximum just below the K-edge energy and a local minimum just above the K-edge energy. Well beyond the K-edge, the transmission increases to 100%. This is illustrated in figure III-2 for $1.8 \times 10^{-2} \text{ gm/cm}^2$ of zinc.*

If x-rays are detected by absorbing them in a material of a suitable thickness, with a K-edge energy somewhat below the K-edge energy of a filter of the type just described, a response function similar to that shown in figure III-4 can be obtained. This response is given by:

$$e^{-\sigma_F(h\nu)X_F} (1 - e^{-\sigma_D(h\nu)X_D}) \quad (1)$$

The first term in the product is the filter transmission function, already shown in figure III-2, and the second term represents the relative detector efficiency, shown in figure III-3. The detector system response function thus obtained is very nearly ideal, being both narrow and relatively constant over the passband.

* X-ray cross-sections were generally obtained from Veigele.²³ These were conveniently available on LLF's CDC Cyber 175 computer. The tables of McMaster, et al.²⁴ were used for some calculations since these include convenient polynomial approximations to the cross sections. The two tables typically differ by less than 10%.

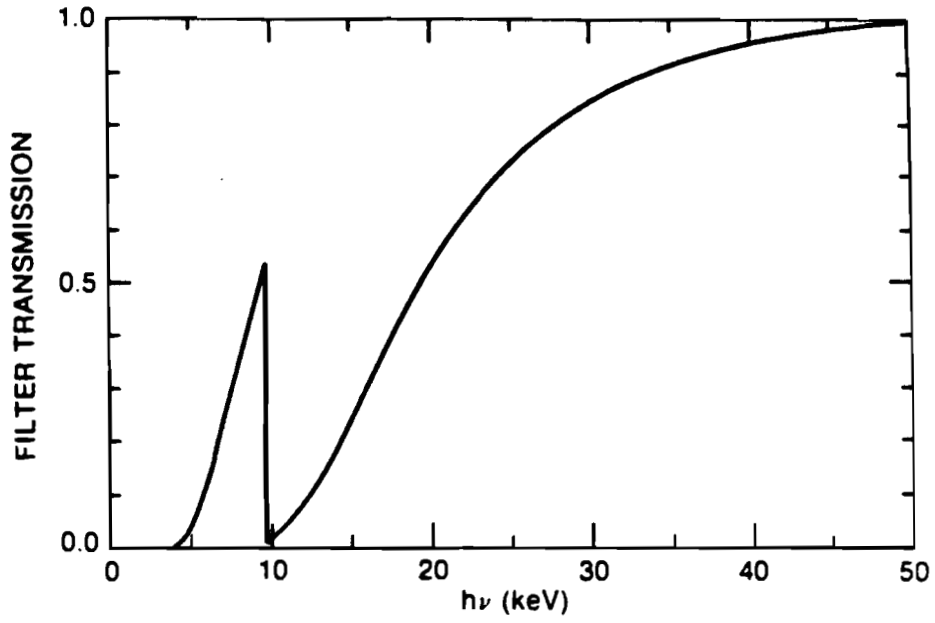


Figure III-2. Transmission of a 0.025 mm Zinc filter.

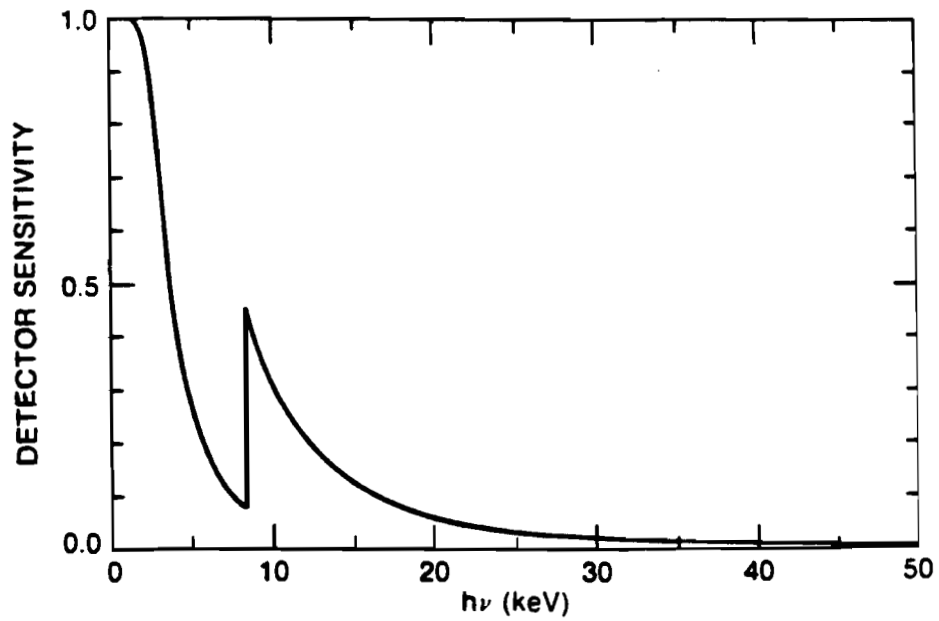


Figure III-3. Efficiency of a 0.002 mm Nickel detector.

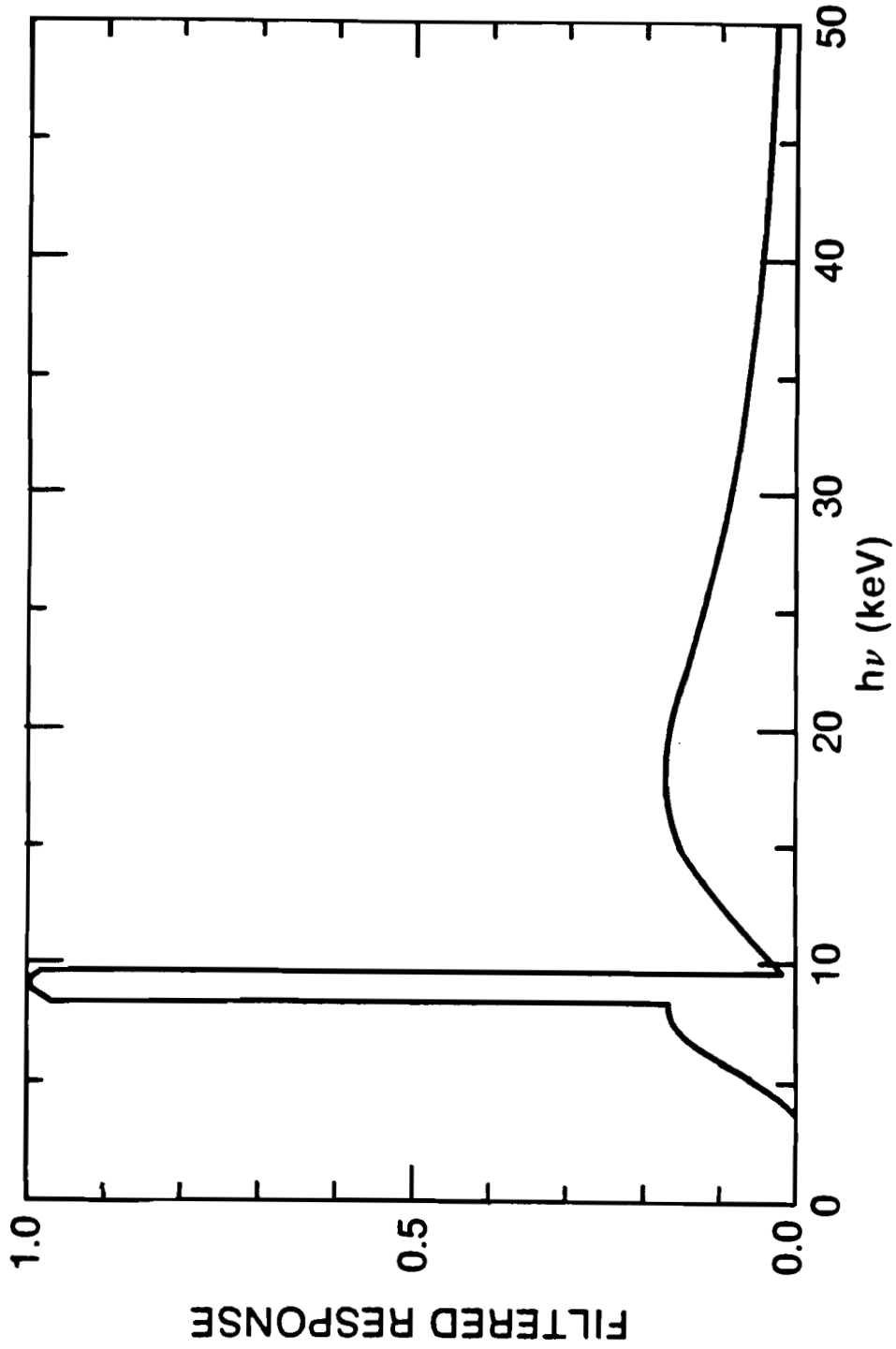


Figure III-4. Idealized K-edge detector response obtained using the Zinc filter of Fig. III-2 and the Nickel detector of Fig. III-3.

The expression (1) assumes that if an x-ray interacts in the detector it loses all of its energy in the detector. In fact, the two processes principally responsible for the total cross section in the energy range of interest here, generally result in a transfer of energy to both electrons and lower energy photons. These photons may escape the detector, resulting in incomplete recovery of the incident photon energy. Whether the secondary photons escape the detector depends on their energy, and hence the particular interaction process, and the detector geometry. The x-ray interaction processes of interest here are photoelectric absorption and Compton scattering.

Photoelectric absorption is the dominant interaction mechanism at low incident x-ray energies. It occurs when an x-ray is absorbed by ejecting a bound electron from an atom. The kinetic energy of the photoelectron is equal to the energy of the absorbed x-ray less the binding energy of the electron to the atom. The kinetic energy of the photoelectron is absorbed within the material through ionization. Recovery of the binding energy depends on the process through which the excited atom relaxes: it may emit an Auger electron, in which case the binding energy is recovered or it may fluoresce, with the fluorescent photon either escaping or being reabsorbed.

The probability of photoelectric absorption is enhanced

when the incident photon has an energy which just exceeds the binding energy of an electron in the atom, thus causing the distinctive discontinuities in the cross section previously mentioned. When an atom fluoresces, the fluorescent photon has an energy slightly less than the edge energy of the shell from which the photoelectron was ejected, hence materials are relatively transparent to their own fluorescent radiation, so even for the case of a semi-infinite material a fraction (see Appendix C):

$$\frac{1}{2} \left(\frac{\sigma_p(h\nu)}{\sigma_T(h\nu)} - \frac{\sigma_p(h\nu) \sigma_T(h\nu')}{\sigma_T(h\nu)^2} \ln \left(1 + \frac{\sigma_T(h\nu)}{\sigma_T(h\nu')} \right) \right) \quad (2)$$

of the fluorescent photons produced will escape the front of the material, where σ_p is the photoelectric cross section, σ_T the total cross section, $h\nu$ the incident photon energy and $h\nu'$ the fluorescent photon energy. For NaI, this fraction is of order 0.25 for $h\nu$ just above the K-edge energy of iodine, but falls off at higher energies.

Compton scattering, the scattering of a photon by a free or loosely bound electron, is important at higher incident photon energies. The energy lost to the electron depends on the scattering angle and from kinematic arguments the energy of the scattered photon is:

$$h\nu' = \frac{h\nu}{1 + \frac{h\nu}{m_e c^2} (1 - \cos\theta)}$$

where θ is the scattering angle of the photon.²⁵ A Compton scattered photon can thus lose from none (0 angle scattering) to all (multiple scatterings followed by photoelectric absorption) of its energy in the detector. Making the detector large helps ensure complete absorption. The problem of indefinite energy loss from Compton scattering can be avoided entirely by working with a detector where photoelectric absorption dominates Compton scattering over the energy range of interest. This is the case with the idealized K-edge detector previously described. In non-ideal cases, choice of a detector with suitably high Z is desirable, since the photoelectric absorption cross section increases as Z^4 whereas the Compton scattering cross section is approximately constant.²⁶

In practice few materials make suitable detectors, since there must be some way of measuring the energy deposited in the material. Materials which permit this include semi-conductors, in which case the number of charge carriers produced by the x-rays in the material is measured, and scintillators, in which the scintillations produced are measured. Because of the limited choice of detector materials the idealized response shown in figure III-4 can generally not be obtained. We consider now the detectors and filtering actually used and the response functions actually obtained.

B. SILICON PIN DETECTORS

Silicon PIN detectors are three layer diodes consisting of a thin N-type layer, an intrinsic layer of variable thickness and a P-type backing. These diodes are used for the low energy (1.5 to 20 keV) channels since their low Z and thin sensitive layer make them insensitive to high energy x-rays. The diodes are reversed biased and x-rays absorbed in the intrinsic layer produce electron hole pairs, resulting in a current in the external circuit. Normally, x-rays reach the I-type layer by passing through the N-type layer, which, since it already has free carriers, acts only as an x-ray attenuator. So it would be expected that the response of a PIN diode would be given by:

$$4.51 \times 10^{-5} e^{-\sigma_{\text{Si}}(h\nu)X_{\text{N}}} (1 - e^{-\sigma_{\text{Si}}(h\nu)X_{\text{I}}}) \quad (\text{pc/keV})$$

where X_{N} and X_{I} are the thicknesses of the N and I type layers respectively and $\sigma_{\text{Si}}(h\nu)$ is the absorption cross section for silicon. The number 4.51×10^{-5} is the charge of an electron divided by the energy required to produce an electron hole pair in silicon. It has been verified experimentally that (3) provides an accurate model of the PIN diode response function, although it was also found that the manufacturer's specification of dead and active layer thickness was not always accurate.²⁷ How this affects the expected signal is described in Appendix B. The active layer thickness of the diodes is sufficient to ensure

absorption of most of the fluorescence photons from photoelectric absorption, but thin enough so that Compton scattering is unimportant.

The filter and diode parameters used in these experiments are shown in Tables V-1 and V-4. Some of the resulting response functions are shown in figures V-3(a-c).

C. NaI SCINTILLATORS

For the high energy channels (20 to 150 keV) where PIN diodes are insensitive, scintillators are used as detectors. A scintillator is a material which converts part of the energy lost by a particle or x-ray traveling through it to visible emission. This visible emission is then detected, generally with a photomultiplier, resulting in a signal proportional to the energy lost in the scintillator. For x-rays, NaI scintillators are preferred, both because the high Z of the material provides a large photoelectric cross section and because NaI yields a large relative pulse height.²⁸

Assuming that an x-ray which interacts in the crystal loses all of its energy in the crystal, the response function for an NaI scintillator coupled to a PMT is given by:

$$C (1 - e^{-\sigma_{\text{NaI}}(h\nu)X_{\text{NaI}}}) \quad (\text{pc/keV})$$

where the constant C depends on the photomultiplier used and the light coupling of the scintillator to the PMT. This constant was determined for each of the PMT-scintillators used here using nuclear sources and the procedure described in Appendix A. The assumption of total energy loss is reasonably good here, since the intermediate energy systems are sensitive where the photoelectric effect dominates the cross section and the high energy systems utilize large crystals.

The filter and detector parameters used in these experiments are shown in Tables V-1 and V-4. Some of the resulting response functions are shown in figures V-5(a-d).

D. FILTER-FLUORESCERS

A modification of the K-edge filtered detector is the filter-fluorescer,²² illustrated schematically in figure III-5. The prefilter, with a K-edge somewhat above the K-edge of the fluorescer, and fluorescer form the idealized K-edge detector system previously discussed. However, rather than detecting the energy deposited in the fluorescer directly, the fluorescence photons which escape the fluorescer are measured. The post filter, of the same material as the fluorescer, is used to attenuate Compton scattered photons from the fluorescer while transmitting most of the fluorescence photons. The properties of the detector have

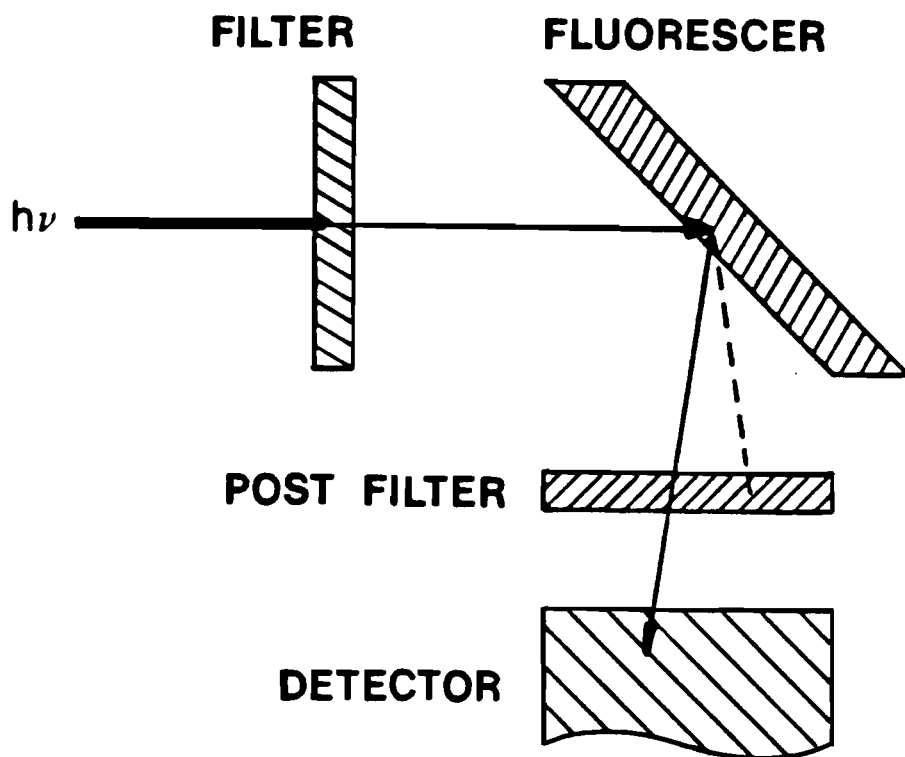


Figure III-5. Filter-fluorescer geometry. The K-edge of the filter is slightly above the K-edge of the fluorescer. The post filter is the same material as the fluorescer and is used to attenuate scattered x-rays.

very little impact on the shape of the response of the system; it is only required that it be efficient at detecting fluorescence photons.

While, referring to equation (2), a substantial fraction of the fluorescence photons produced in the fluorescer escape the front of the fluorescer, in practical geometries it is only possible for the detector to intercept a small portion of the 2π solid angle. For example, with a 25 mm minor diameter fluorescer, a 25 mm diameter detector could reasonably be placed 50 mm from the center of the fluorescer. For this case about 3% of the approximately 25% of the fluorescence photons escaping the fluorescer would be collected, so that a filter-fluorescer would have about 1% of the sensitivity of a similarly filtered K-edge system. Based on experience with the K-edge systems, such a low sensitivity would yield a marginal signal in the case of moderate energy (20-30 keV) channels and an unusable signal at high energies in the case of the GDL experiments.

The low sensitivity of the filter-fluorescer system also requires that considerable care be exercised in their design and construction to prevent either direct or scattered x-rays from the target or stray fluorescence from the assembly surrounding the fluorescer from reaching the detector, since any of these sources could result in a signal which could exceed the desired fluorescence signal. Because

of these difficulties and their low sensitivity, it was decided not to implement filter-fluorescer detectors.

CHAPTER IV
DATA REDUCTION AND ERROR ANALYSIS

A. SPECTRAL UNFOLDING

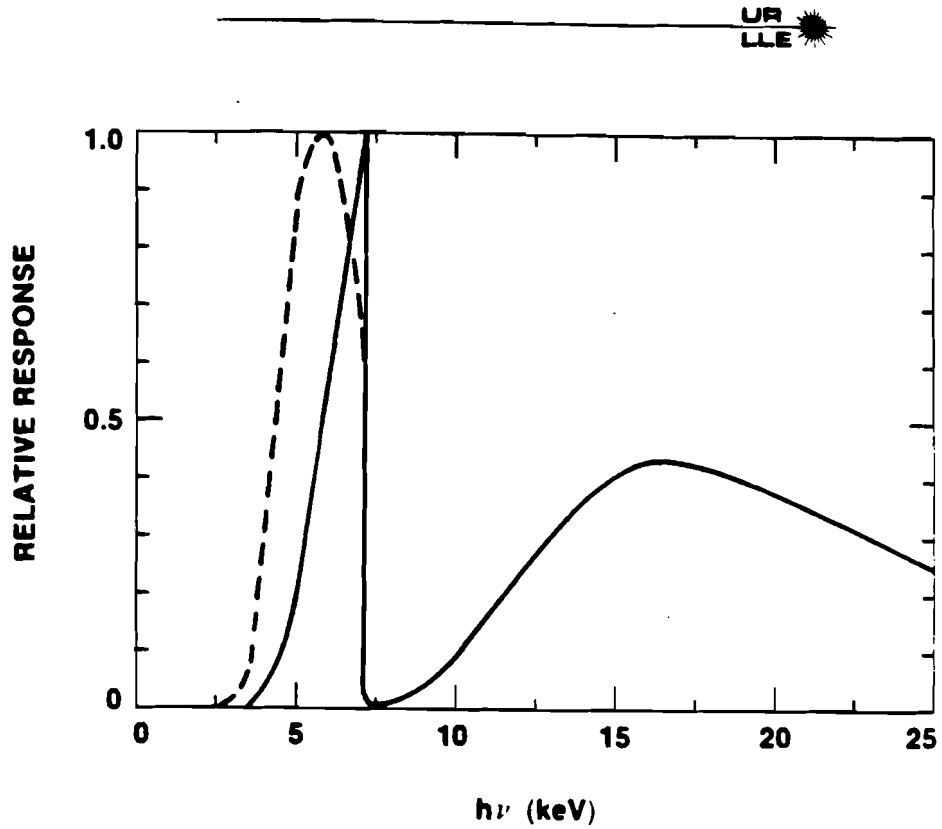
If the K-edge detectors were reasonably narrowband ($\Delta h\nu \ll h\nu$) and had a reasonably flat response, then the signal from each detector would be proportional to $\Delta E \propto dE/dh\nu \Delta h\nu$. Hence we would have a measurement of $\Delta E/\Delta h\nu \propto dE/dh\nu$ at several values of $h\nu$ determined by the detectors. By using a suitable interpolation method an approximation to $dE/dh\nu$ could be obtained over the measured energy range.

As is apparent from the plots of the detector sensitivities in figures V-3(a-c) and V-5(a-d), the detector responses are neither flat nor narrow. If $dE/dh\nu$ decreases sufficiently rapidly with increasing $h\nu$, the effective response of a detector becomes narrow, but still remains non-uniform as illustrated in figure IV-1.

Since the measurement is inherently an integral one, that is the signal from each detector is given by:

$$q_i = \int_0^{\infty} R_i(h\nu) \frac{dE}{dh\nu} dh\nu$$

K-EDGE DETECTOR RESPONSE



E2408

Figure IV-1. The response of a K-edge filtered diode. At 1 keV an effectively narrowband response is obtained (dashed curve).

a method of specifying $dE/dh\nu$ globally is required. One simple means of doing this is to use a multi-group approach, dividing the spectrum up into bins, with $dE/dh\nu = \text{constant}$ in each bin. The magnitude of $dE/dh\nu$ in each bin would be determined by minimizing the sum square error:

$$SSQ = \sum_i (Q_i - q_i)^2 / \sigma_i^2 \quad (2)$$

The maximum number of bins that could be used would be equal to the number of detectors in use, in which case $SSQ = 0$ would always be obtained.

Several difficulties exist with this scheme. One is that the partitioning of the spectrum into bins is completely arbitrary and a different solution will be obtained for each choice of partitioning. Another difficulty is that spectra specified in this manner are cumbersome to compare, either with each other, since the energy in each group must be compared for each spectrum, or with theory, which often provides the spectrum in terms of electron temperatures.

It would be preferable to be able to specify the spectrum with a family of functions of $h\nu$ and some small number of parameters. If the functions are chosen on the basis of the physics of the radiation, the totally arbitrary nature of the multi-group method is avoided. In addition the parameters would correspond to identifiable physics, making interpretation of the data simpler. Keeping the number of

parameters small makes comparison of spectra simpler. We have chosen to use this approach, using functions of the form:

$$\frac{dE}{dh\nu} = \sum_{j=1}^K N_j e^{-h\nu/T_j} \quad (3)$$

where T_j and N_j are the parameters used to minimize SSQ in equation (1). This particular choice of functional form is motivated by the fact that the bremsstrahlung radiation from a Maxwellian electron distribution is given by:²⁹

$$\frac{dE}{dh\nu} = C z^2 \left(\frac{1}{T_e}\right)^{1/2} n_e n_i e^{-h\nu/T_e} \quad (4)$$

If the electron distribution actually consists of K Maxwellians, then the parameter T_j in equation (3) represents the temperature of the corresponding component. Since the measurement is both time and space integrated and the actual electron distribution is not known, the T_j should be only loosely interpreted as representing the actual electron temperatures.

The multi-Maxwellian model may appear to be overly restrictive. However, numerical simulations of resonance absorption¹⁷ and the Raman⁵ and $2\omega_p$ instabilities⁴ predict electron distributions which are approximately Maxwellian. Furthermore, we find that the x-ray spectra predicted by the hydrodynamic code SAGE, which incorporates a phenomenological hot electron source, can be reasonably approximated with

a two Maxwellian model. This indicates that, despite time and space averaging, distinct electron distributions produce distinct x-ray components. Finally, we find that, for a suitable choice of K , good fits to the data are obtained.

To obtain a feel for the functional form of the spectrum, it is useful to plot it on a semi-log scale as in figure IV-2. Equation (3) then appears as a series of straight line segments, each segment corresponding to one of the terms in the sum. The $h\nu = 0$ intercept of each segment corresponds to the parameter N_j . $-1/T_j$ is proportional to the slope of each segment. While the energy radiated by a given component is $N_j T_j$, recall that by using Brueckner's model, the energy in the corresponding electron distribution is simply proportional to N_j .

B. LEAST SQUARE REDUCTION

One of the problems with the model of equation (3) is that it is non-linear in the parameters. In the linear case, least square regression reduces to a matrix inversion and a unique solution is obtained. In the non-linear case a solution must generally be obtained using an iterative method and there may exist multiple solutions. For our model, if one solution is found there are $K!$ trivially different solutions corresponding to the permutations of the

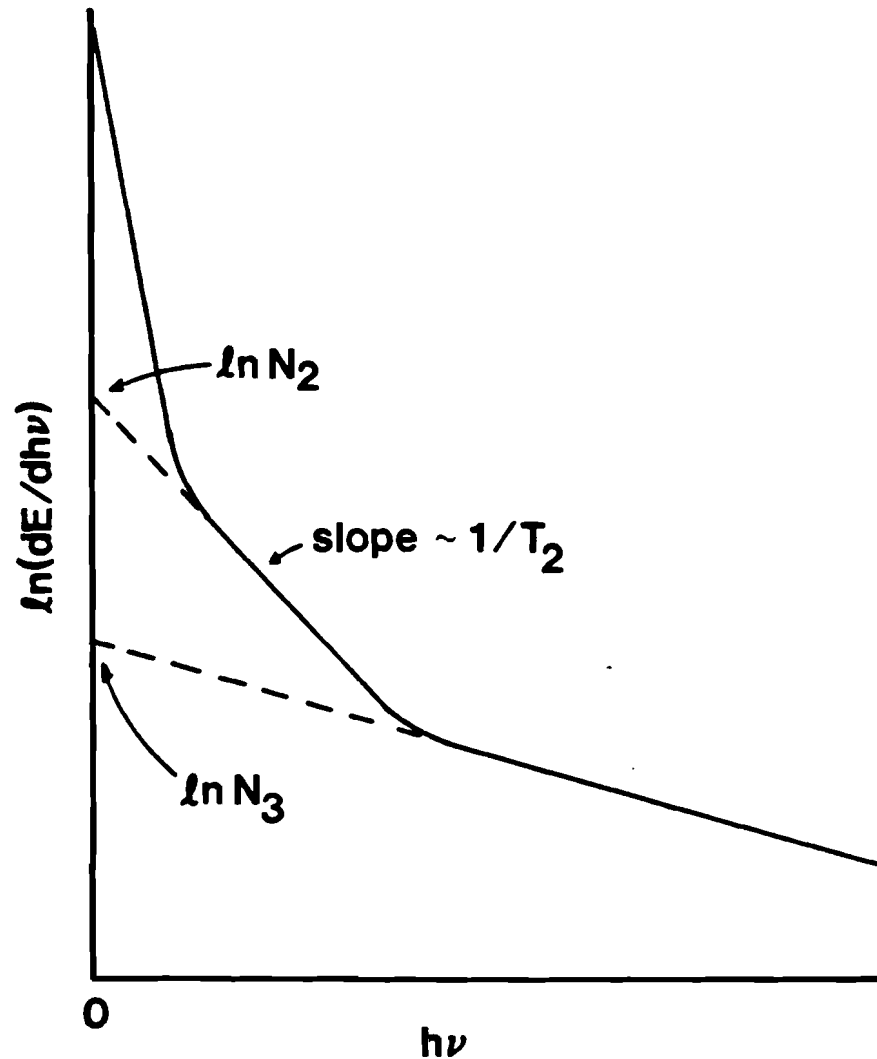


Figure IV-2. When plotted on a semi-log scale the multi-Maxwellian spectrum appears as a series of straight line segments. The slope of each segment is proportional to $1/T$ and the $h\nu = 0$ intercept is determined by N .

indexes. In addition, there may be multiple local minima in the SSQ, so care must be exercised to ensure that the iterative method finds the best solution.

Data reduction is accomplished with the FORTRAN V program MAXSPEC, running on LLE's CDC Cyber 175 computer. At the heart of this program is the IMSL routine ZXSSQ, which uses "a finite difference, Levenberg-Marquardt routine" to solve the non-linear least square problem.³⁰ To reduce the computational load on ZXSSQ and increase the stability of the solution, we have utilized the fact that the model is linear in N_j and fit these parameters using conventional linear least square techniques.

The estimate of the error in the measured data caused by the uncertainty in filter foil thickness, causes an additional complication in the reduction procedure. This is because the effect of foil thickness error on the data is a function of the measured x-ray spectrum. Thus, the appropriate data weighting is a function of the solution, and in order to obtain an unbiased solution, the weights and the parameters T_j and N_j must be obtained self-consistently.

To this end the reduction procedure works as follows:

1. Input an initial guess for the T_j , T_{0j} .
2. Call ZXSSQ. For any choice of T_j the residuals $(Q_i - q_i)$ are provided to ZXSSQ by subroutine RESIDF. The residuals are weighted, but the error due to filter thickness is

ignored. RESIDF computes the N_j on the basis of a linear least square fit using the supplied T_j . Starting at T_{0j} , ZXSSQ iterates until its convergence criteria are satisfied and returns the solution T_{1j} .

3. Call ZXSSQ again, with T_{1j} as initial parameter estimates. This time the residuals are supplied by subroutine RESID, which includes in the weighting factors the filter thickness errors. The N_j are still obtained by linear least squares, but the procedure must be repeated reweighting each time until the N_j and weights are self-consistent. Convergence of the N_j is considered obtained when on successive iterations the weights differ by less than 1 in 10^{10} . This exceptional accuracy is required to ensure that ZXSSQ is not "confused" by artificially introduced roughness in the residuals. ZXSSQ iterates until its convergence criteria are satisfied and returns the solution T_j .

Step 2 is included to avoid excessive computation should the initial guess of the parameters T_{0j} be very far off. RESIDF is a much simpler and much faster subroutine than RESID and in most cases the solution obtained in step 2 will be very close to the self-consistent solution, minimizing the number of calls to RESID.

The filter thickness error contribution to the error in the data is computed using:

$$\Delta q_i = \frac{d}{dX_F} \left(\int_0^{\infty} R_i(h\nu) \sum_{j=1}^K N_j e^{-h\nu/T_j} \right) \Delta X_F$$

The derivative can be performed analytically, but the integrals must be performed numerically. It will be noted that the N_j can be removed from within the integrals, so for fixed T_j the error is a function of the N_j only, thus the integrals need be computed only once for each call to RESID.

C. ERROR ANALYSIS

Having obtained estimates of the parameters T_j and N_j , it is useful to have some idea of their expected variability. Unfortunately, because the spectral model is non-linear in the T_j 's, the usual results used in linear least squares* analysis to obtain individual and joint confidence intervals for the parameters do not apply. While it is possible to obtain a "correct" joint confidence interval in the non-linear case, its actual confidence level will only be approximate. It is always possible to linearize the problem about best fit and then apply the results of the linear theory. If the errors are sufficiently small, then the confidence intervals obtained will approximate those of the original non-linear problem. Although the errors encoun-

*These results are covered in numerous texts. Draper and Smith³¹ is particularly useful since it provides a discussion of non-linear least square fitting.

tered in these experiments are not particularly small, linearization has been used anyway, since there is no reasonable alternative.

The least square problem involves minimizing $SSQ = \underline{W}(\underline{Q}-\underline{g})(\underline{W}(\underline{Q}-\underline{g}))'$, where \underline{g} is a vector of observations, \underline{Q} is a vector of predicted values of the observations and \underline{W} is a diagonal weight matrix. If the model is linear, then $\underline{Q} = \underline{X}\underline{P}$ where \underline{P} is a vector of parameters to be estimated and \underline{X} is a matrix describing the predictor variables for each observation. Then the solution \underline{P}_0 which minimizes SSQ is $\underline{P}_0 = (\underline{X}'\underline{V}^{-1}\underline{X})^{-1}\underline{X}'\underline{V}^{-1}\underline{g}$, where $\underline{V}^{-1} = \underline{W}'\underline{W}$ is a matrix with diagonal elements equal to the reciprocal of the variance of the corresponding element of \underline{g} . The matrix $(\underline{X}'\underline{V}^{-1}\underline{X})^{-1}$ is the variance covariance matrix. Its diagonal elements are the variances of the corresponding element of \underline{P}_0 while the off diagonal elements provide the covariances.

If the \underline{P}_j are uncorrelated then the individual confidence intervals of the \underline{P}_j provide a reasonable estimate of the joint confidence region. The correlation coefficient $\rho_{ij} = \text{cov}(\underline{P}_i, \underline{P}_j) / (\text{var}(\underline{P}_i)\text{var}(\underline{P}_j))^{1/2}$ can be obtained from the variance covariance matrix. It ranges from -1 to 1 with a value of 0 implying that \underline{P}_i and \underline{P}_j are uncorrelated. If, however, \underline{P}_i and \underline{P}_j are strongly correlated, then the individual confidence intervals will be misleading. In this case, the joint confidence region should be used. The situation

is illustrated in figure IV-3.

In these experiments, using the multi-Maxwellian spectral model, the linearized variance covariance matrix shows that T_i and N_i have a strong negative correlation. This is not surprising, since referring to an example spectrum, figure IV-4, it is apparent that if, for example, T_2 is increased, the corresponding intercept N_2 will necessarily decrease. The different temperature components which comprise the spectrum are, however, largely uncorrelated. Notwithstanding the previous comment on the use of individual confidence intervals under these circumstances, the error bars placed on the parameter estimates here are obtained on an individual basis. This is mainly because it is impractical to present a joint confidence region for any spectrum with $K > 1$.

In light of the foregoing, the following points should be kept in mind regarding the error bars placed on T_j and N_j :

- 1) the error bars on T_j and N_j are approximate and obtained by linearizing about the best fit obtained as described in the previous section,
- 2) the error bars given are plus or minus one standard deviation,
- 3) T_j and N_j have a strong negative correlation so that an increase in T_j will result in a decrease in N_j .

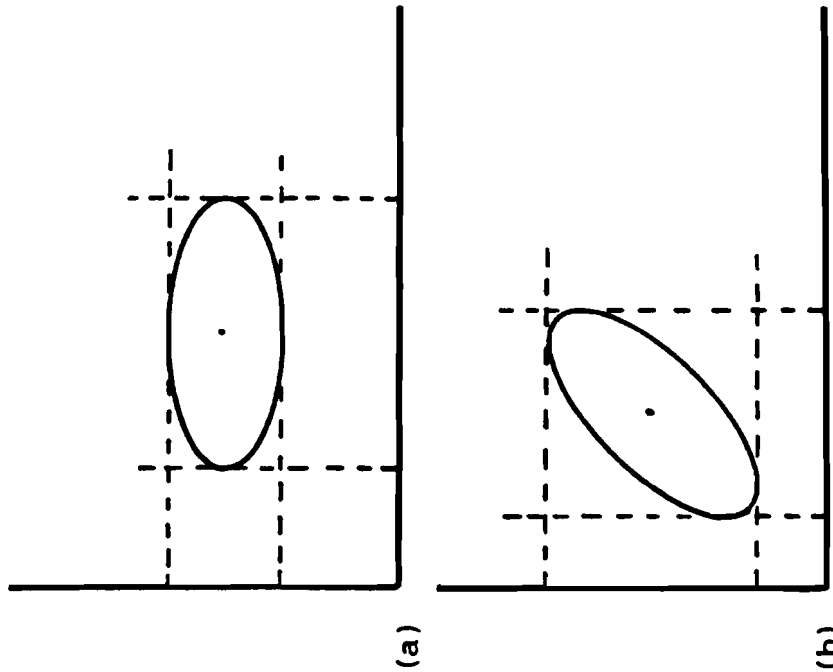


Figure IV-3. If the parameters are uncorrelated (a) then the joint (ellipse) and individual (dotted box) confidence limits are approximately equivalent. This is not the case if the parameters are correlated (b).

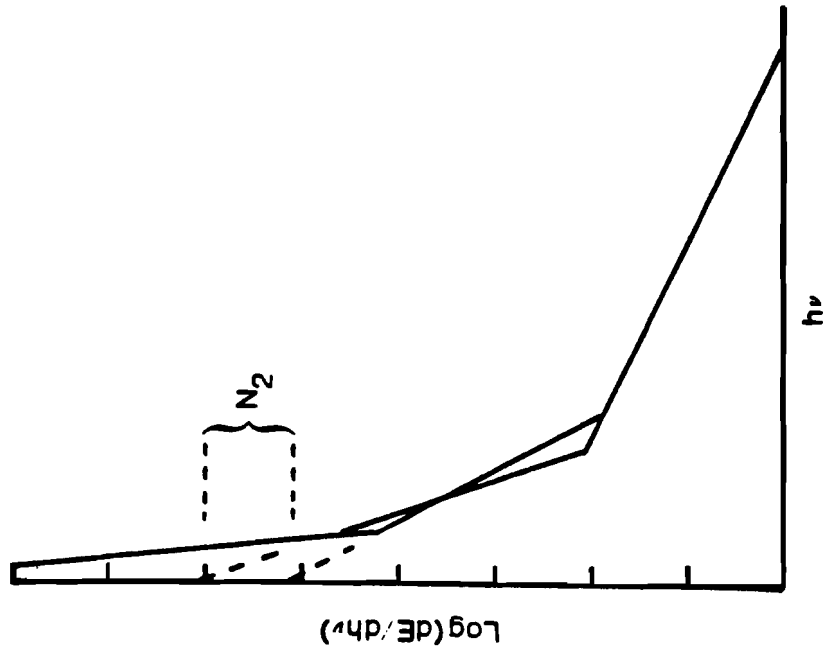


Figure IV-4. A relatively small error in the determination of T (T_2 in the figure) will result in a significant error in the corresponding N .

D. SOURCES OF ERROR

The weights W_{ii} required by the weighted fitting procedure and to obtain the confidence intervals for the P_i require that the variances, σ_i , of the data g_i be known. If proper repeat measurements are available then these can be obtained from the data or if the model can be assumed correct they can be obtained from the residual error in the fit. Neither of these approaches is satisfactory here, since true repeat measurements cannot be obtained and the assumption that there is no lack of fit would be optimistic. For these reasons, the variances of the g_i have been estimated.

The error in g_i can be attributed to four main sources: uncertainty in the thickness of the filter foils, uncertainty in the calibration of the detectors, uncertainty in the solid angle subtended by the detectors, and noise. Since, once installed, the detectors remain unaltered, the first three of these errors are to a certain degree systematic. However, from detector to detector these errors are at least approximately random and uncorrelated and so will contribute to the residual error. Only the noise error varies from shot to shot. For this reason, it is to be expected that the scatter in the data obtained under nominally identical conditions will be smaller than the error bars would imply.

Foil thickness error and solid angle error can be

estimated quite simply, since they involve only the measurement of lengths or, in the case of the foils, mass. Calibration error is discussed in Appendix A and B. Noise error is somewhat difficult to determine. It has basically been assumed to be small compared to the calibration and foil thickness errors and so not a major contributor to the total error.

For a weighted least square fit the quantity $SSQ_{\min}/(p-2K)$, referred to as χ^2 since in the linear case it has a χ^2 distribution, has an expectation value of one if there is no lack of fit and the variances of the q_i are correct. In principle χ^2 provides an indication of the quality of fit. Since in these experiments the variances are not accurately known, χ^2 is primarily useful when comparing the quality of fit between shots or when choosing the number of Maxwellians, K , to use. The most useful method of judging quality of fit is to plot the data as shown in figures V-7(a-c) and V-8(a-c).

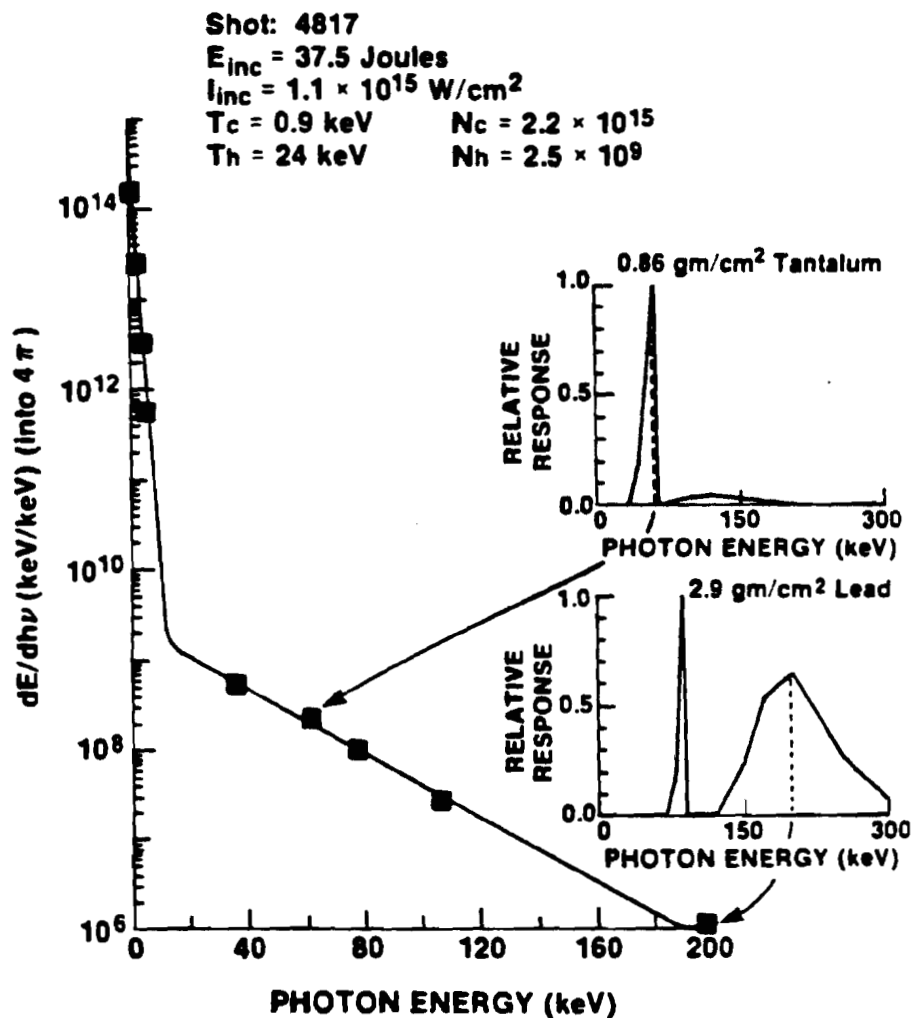
These plots require some explanation. The solid curve is the representation of the multi-Maxwellian spectrum obtained by the non-linear fitting program MAXSPEC. Since the response functions of the detectors are not generally narrow there is, in the strict sense, no way to locate the data on a plot of this type. This has been done anyway by plotting the data from detector i at:

$$(h\nu_i', \frac{Q_i}{Q_i} \frac{dE}{dh\nu} \Big|_{h\nu_i'})$$

where the frequency ν_i' is chosen such that half of Q_i is produced by x-ray photons with energy less than $h\nu_i'$. This is illustrated in figure IV-5, where the insets show the spectrally weighted responses of two detectors and the vertical dashed lines are at $h\nu_i'$. This method of plotting the data makes it relatively easy to find a saturated detector or determine if the number of Maxwellians, K , is too small. However, because $h\nu_i'$ is a function of the fitted spectrum, it must be remembered that it is not possible to simply "draw" alternative curves through the plotted points.

TWO TEMPERATURE X-RAY SPECTRUM AND RELATIVE CHANNEL RESPONSE

UR
LLE 



E1909

Figure IV-5. X-ray spectrum showing how data is plotted. The insets show the effective response of two channels. The vertical dashed lines indicate the energy at which the data is plotted.

CHAPTER V

EXPERIMENT

The x-ray continuum measurements described were a part of a larger effort to investigate coronal physics or the physics of laser plasma interactions under conditions of interest to laser fusion experiments. This effort commenced when it was demonstrated, using the GDL laser, that a 1.05 μm laser could be efficiently frequency tripled to a wavelength of 0.35 μm . The coronal physics program on GDL was intended to ascertain if converting a multiple beam laser system to 0.35 μm to do further laser fusion studies would be worthwhile.

During the course of the 0.35 μm experiments, one of the frequency conversion crystals was damaged and had to be removed from the system for repairs. Rather than let the laser system lie idle, it was decided to perform experiments at 1.05 μm . Previous x-ray continuum measurements done at LLE at this wavelength had produced indifferent results, in part because so many x-rays were produced that the detectors saturated. However, the intensity on target would now be considerably lower, reducing the chance that saturation

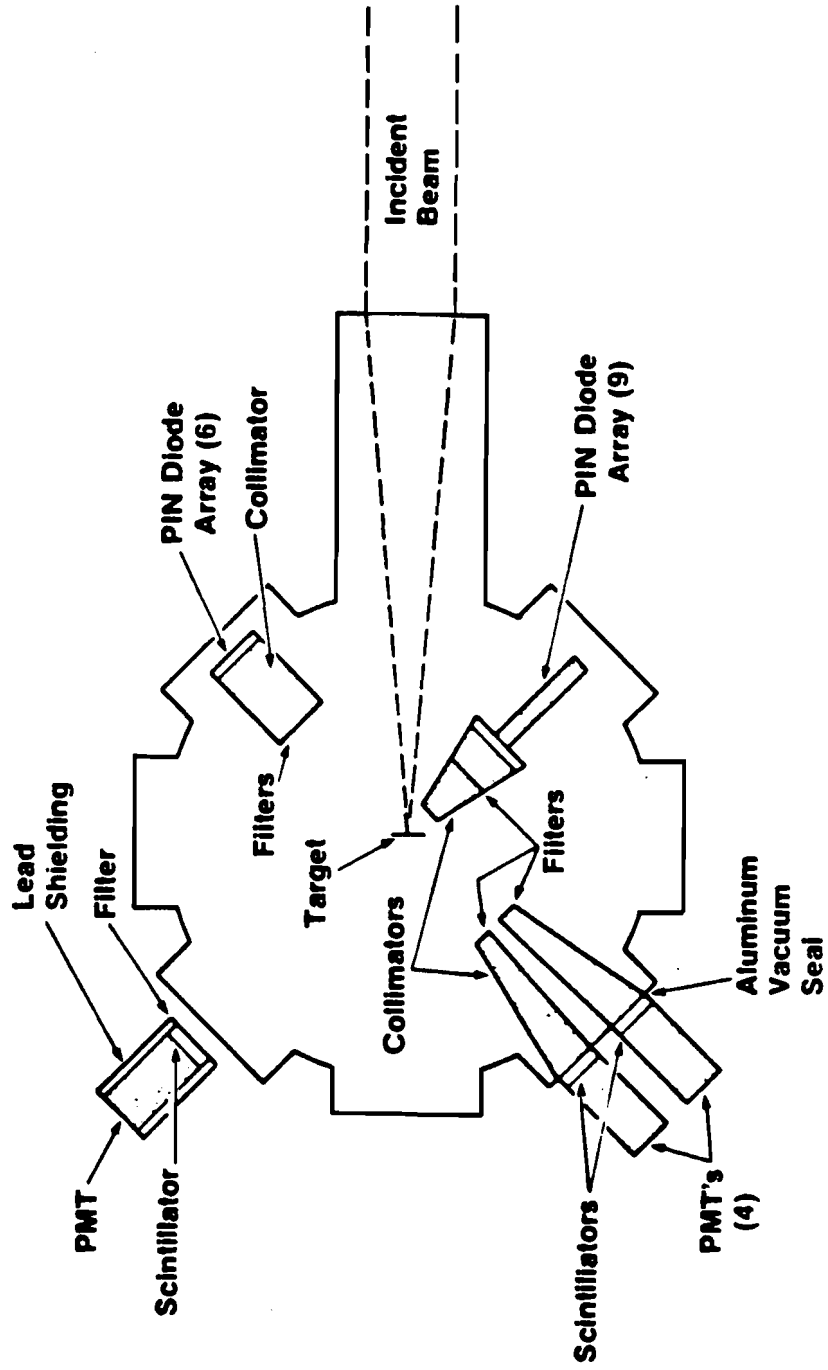
would be a problem. Because of the limited time available and very different x-ray signals, most of the data obtained was a total loss, but several shots could actually be reduced. The results were sufficiently interesting that additional 1.05 μm experiments were later performed on GDL.

At the conclusion of the GDL coronal physics program it was realised that a comparable study had never been done on the 24 beam OMEGA system. Since it was now anticipated that at least six beams of this system would be converted to 0.35 μm , it seemed desirable to repeat the experiments on OMEGA in order to provide a reference data base for future 0.35 μm experiments.

A. GDL EXPERIMENTS

GDL is a single beam frequency tripled Nd-glass laser. It has been described in detail by Seka et al..³² The target area layout is illustrated in figure V-1. All of these experiments utilized planar plastic (CH) targets with the beam impinging on the target at near normal incidence. Targets were large, effectively of infinite mass. The intensity on target was varied by changing focal spot size and laser energy. Focal spot diameters ranged from approximately 100 to 300 μm . Laser energy ranged from 20 to 40 Joules. Pulse lengths were either 0.5 or 0.9 ns.

PHYSICAL CONFIGURATION **JR**
LLE



E1503

Figure V-1. GDL target area configuration.

The silicon PIN diodes were mounted in two lead collimated and shielded arrays, one positioning the diodes 11 cm from the target, the other 43 cm from the target. Both arrays utilize thin beryllium foils to assure a light tight assembly. Magnets mounted in front of the filter foils minimize foil fluorescence caused by electron impact with the foils. The diodes used in these experiments were all Quantrad model 025-PIN-125, having a nominal 25 mm^2 area with dead and active layer thicknesses specified at 0.75 and 125 μm respectively. The diode arrays are shown schematically in figures V-2 a and b. The filtering for each PIN channel is shown in Table V-1. Several of the corresponding response functions are plotted in figures V-3(a-c).

For these experiments six filtered NaI scintillator detectors were used. Four of these were NEI model 6/1A-1.5/1HG detectors consisting of 0.1 mm thick by 1 inch diameter NaI crystals integrally mounted to EMI model 9843KB/FL photomultipliers. These detectors were mounted in a collimator array fastened to the target chamber. The array was 45 degrees from the laser axis and faced the rear of the target. The cast lead collimators extended into the chamber with the K-edge filters mounted on the target end. The detectors were mounted outside the chamber, separated from the vacuum by a 1 mm aluminum window. Lead apertures could be placed in the collimators when required to prevent detector saturation. The assembly is illustrated in figure

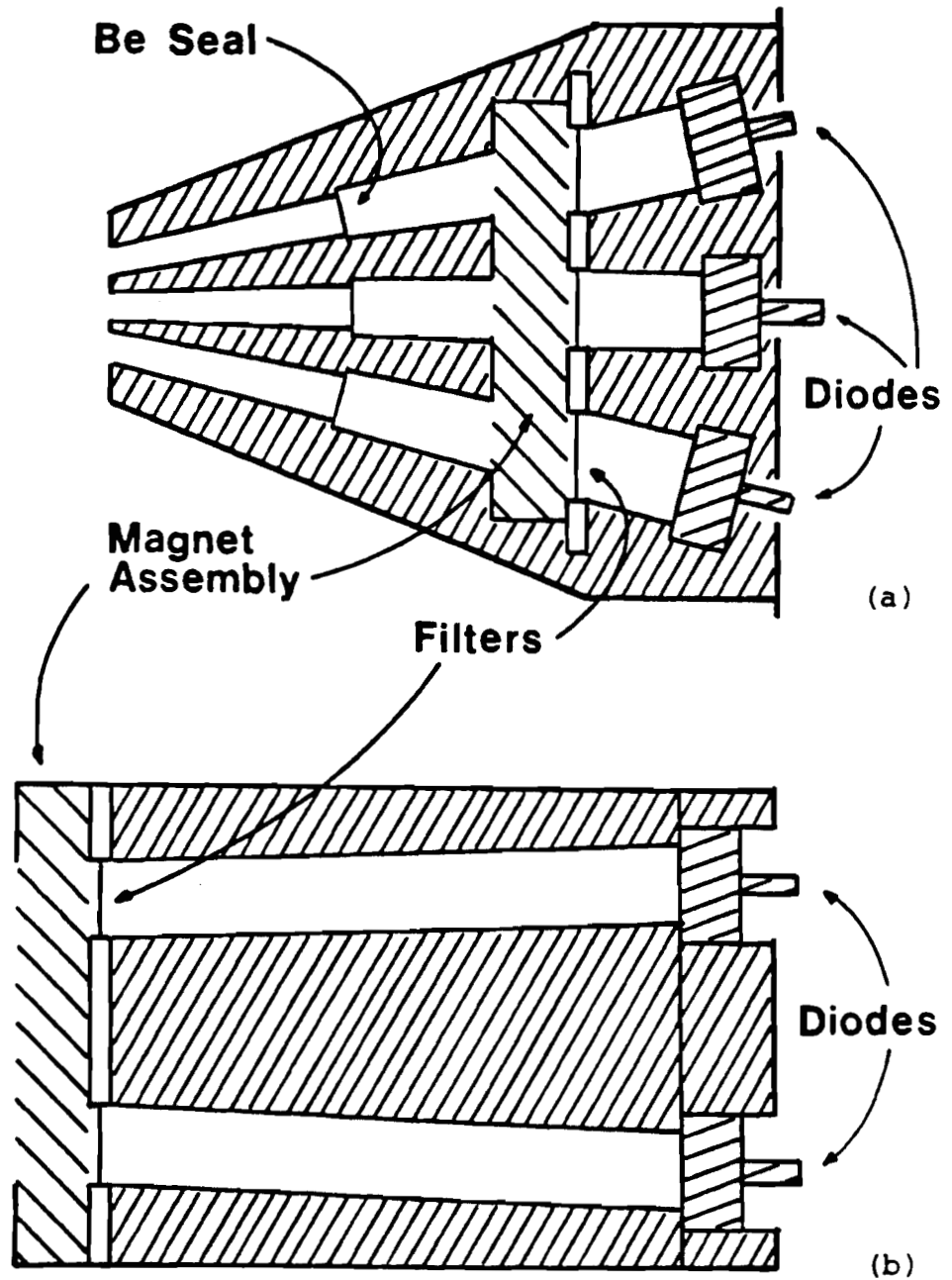


Figure V-2. Schematic illustration of GDL PIN diode collimator assemblies. (a) placed the diodes as close to the target as possible and was used for the higher energy channels. (b) placed the diodes further from the target and was used for low energy channels.

TABLE V-1. GDL K-EDGE FILTERED DETECTOR SYSTEM PARAMETERS

Filter Material	Filter Thickness	K-edge (keV)	Detector Material	Detector Thickness	Detector Type
Al	10 μ m	1.6	Si	125 μ m	PIN
Cl (Saran)	12	2.8	Si	125	PIN
Ti	27	5.0	Si	125	PIN
Fe	25	7.1	Si	125	PIN
Ni	20	8.3	Si	125	PIN
Zn	51	9.7	Si	125	PIN
Y	100	17.0	Si	125	PIN
Mo	113	20.0	Si	125	PIN
Al	1000	1.6	NaI	1 mm	PMT
Sn	100	29.2	NaI	1	PMT
Ta	515	67.4	NaI	1	PMT
Pb	1.0 mm	88.0	NaI	1	PMT
Fe	6.4	7.1	NaI	50	PMT
Pb	2.5	88.0	NaI	50	PMT

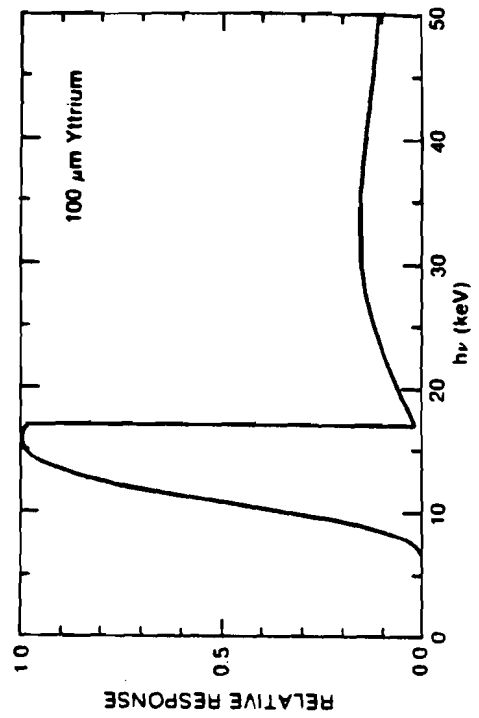
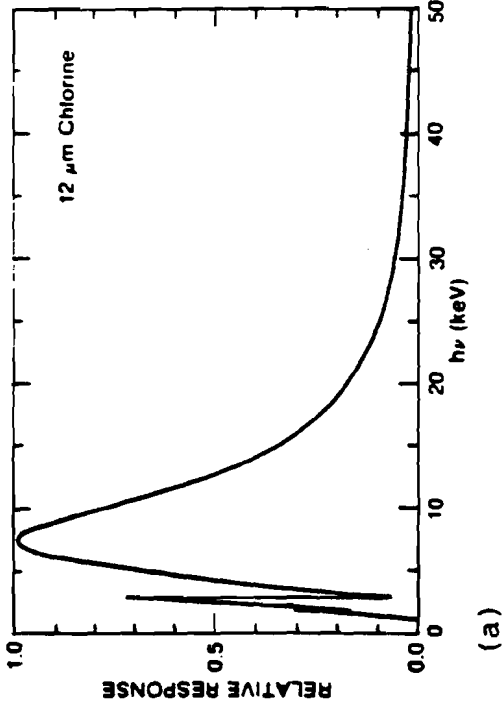
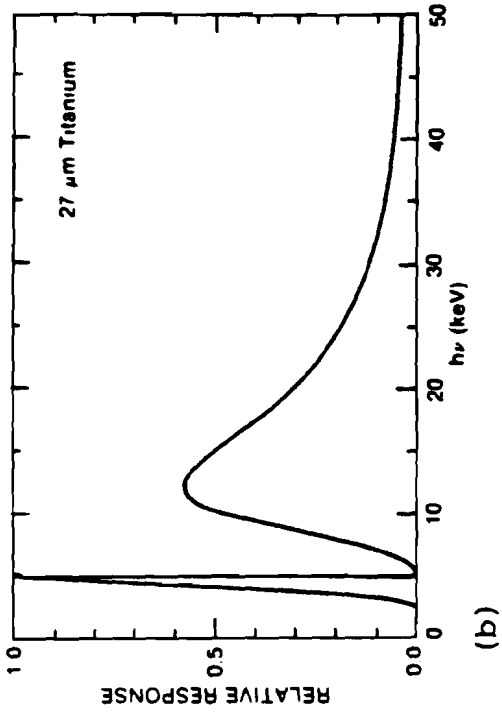


Figure V-3. Response functions for several of the filtered PIN diodes used for the GDL experiments.

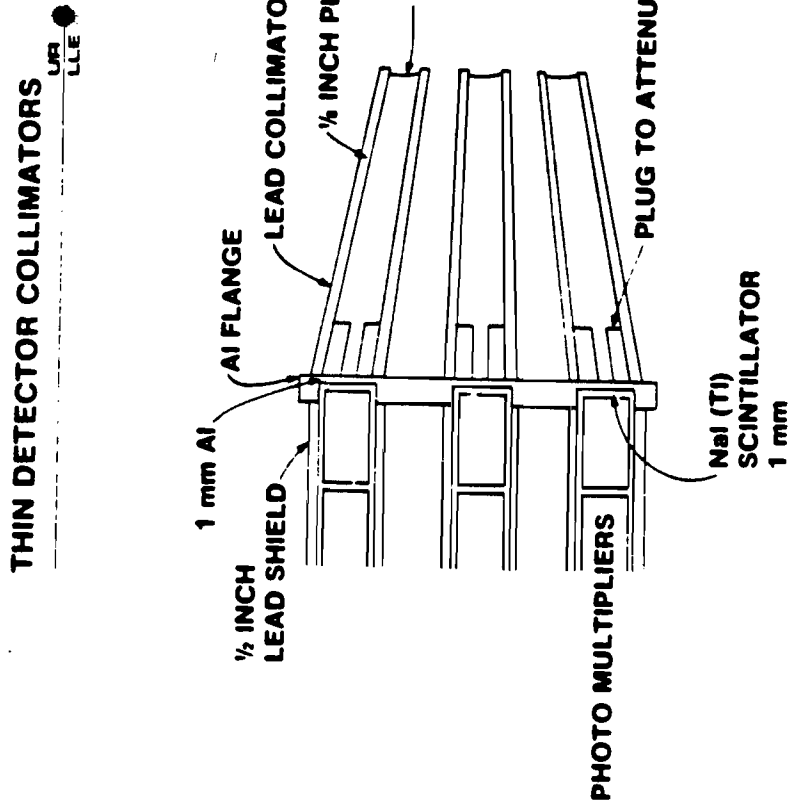
V-4.

The remaining two detectors were Harshaw model 8S8/2 detectors consisting of 2 inch thick by 2 inch diameter NaI crystals integrally mounted to RCA model 6342A photomultipliers. These detectors were mounted outside the tank and were shielded, but uncollimated. These detectors viewed the target through either a 1/2 inch thick aluminum port or the 1/4 inch thick steel tank wall.

The filtering used for the various NaI scintillator detectors is shown in Table V-1. Several of the response functions are plotted in figures V-5(a-d).

The signals from the detectors were acquired with LeCroy 2249W gated integrating analog to digital converters. These were interfaced to a Digital Equipment Corp. (DEC) LSI-11/2 computer through CAMAC. LeCroy 8302 CAMAC readable hex attenuators and fixed attenuators were incorporated as required to prevent A/D saturation. The typical configuration is illustrated in figure V-6. Acquisition software was written in the FORTH programming language running under the RT-11 operating system. Oscilloscope monitoring was used to check for saturated or noisy signals.

Since the GDL 0.35 μm experiments were the first of the x-ray continuum measurements described in this thesis, they were repeated several times as improvements such as the



E1394

Figure V-4. Collimator assembly used for the 1 mm NaI detectors on GDL.

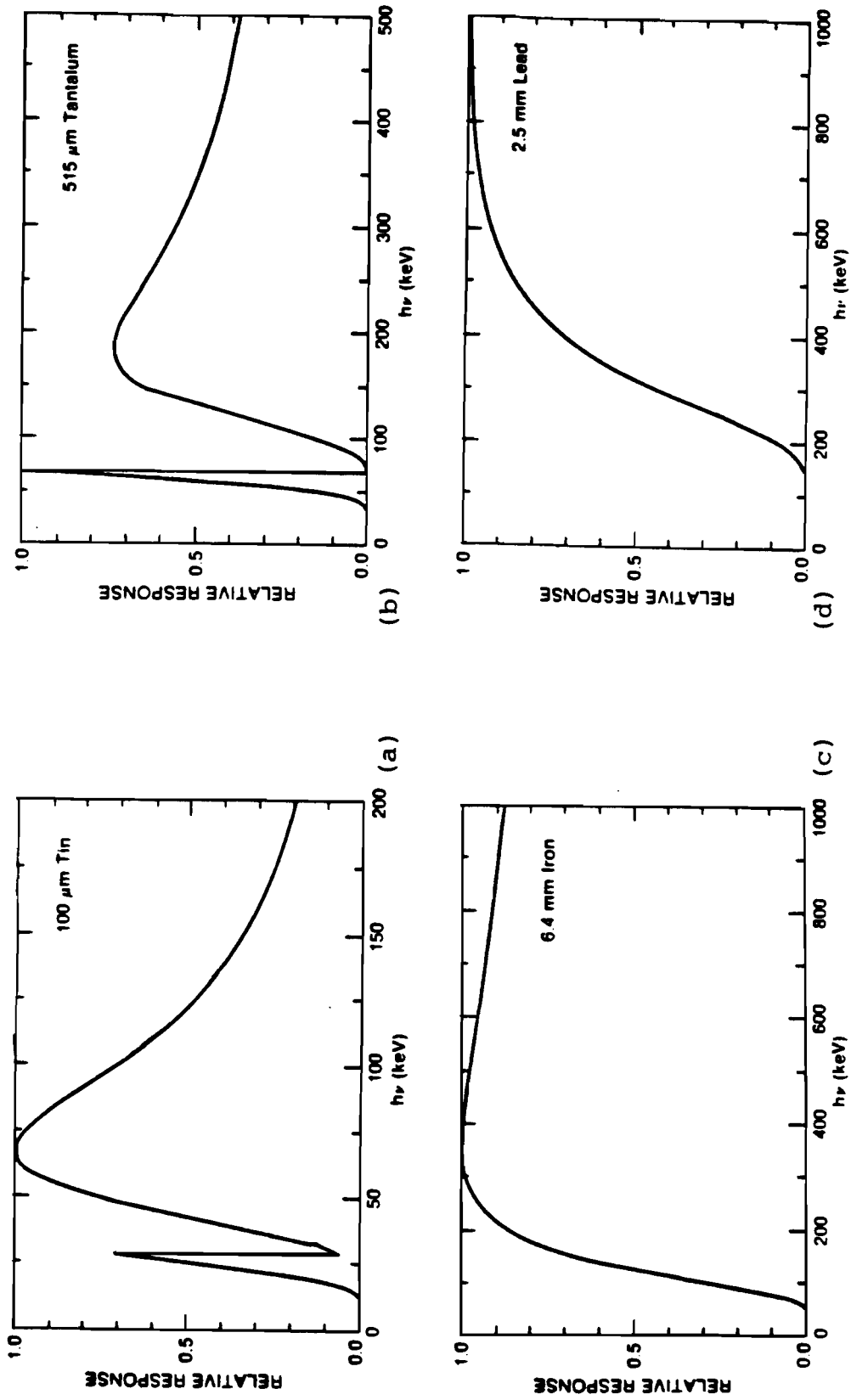


Figure V-5. Response functions for several filtered NaI detectors. (a) and (b) are 1 mm detectors. (c) and (d) are 50 mm detectors.

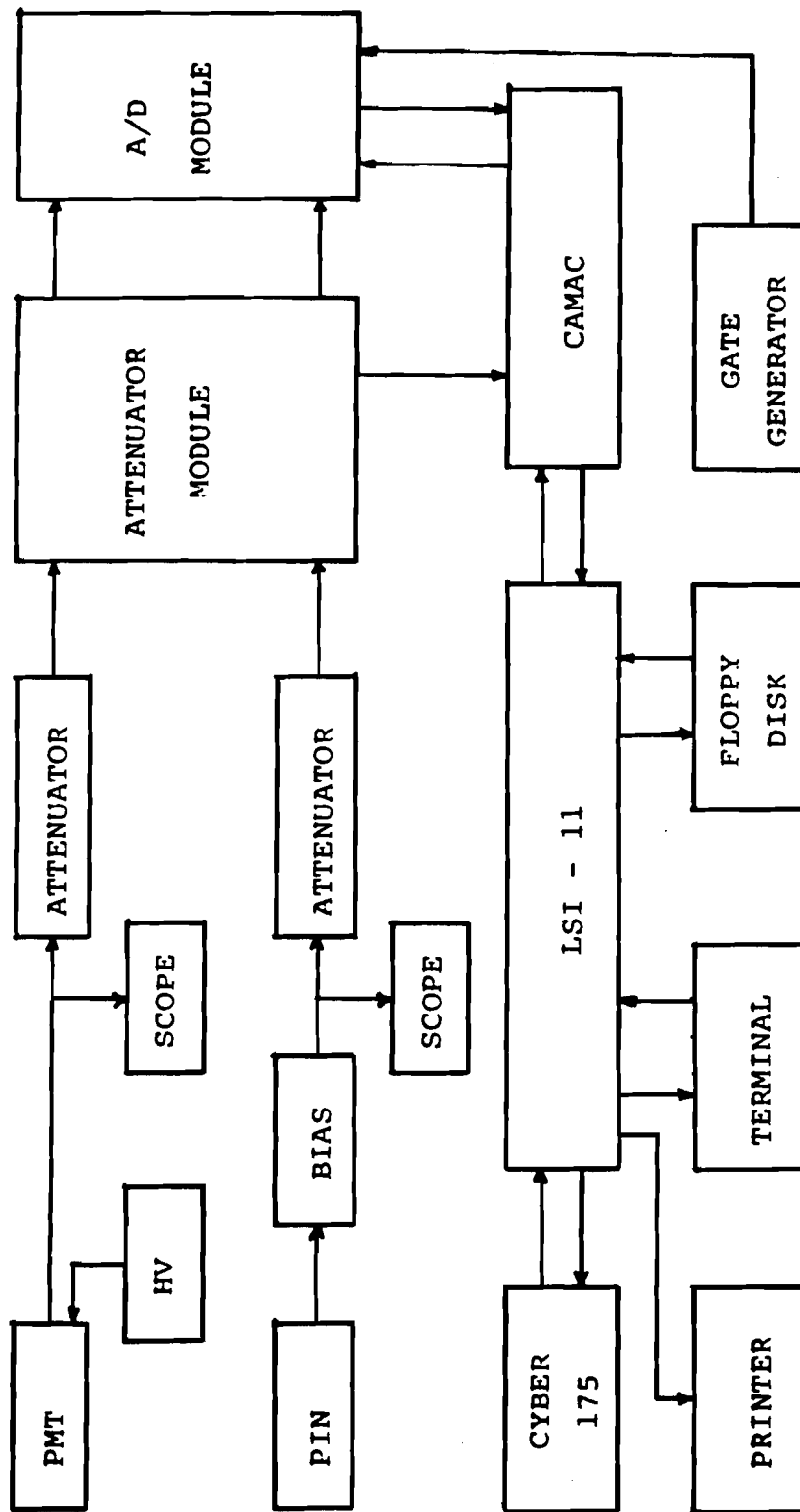


Figure V-6. Data acquisition configuration.

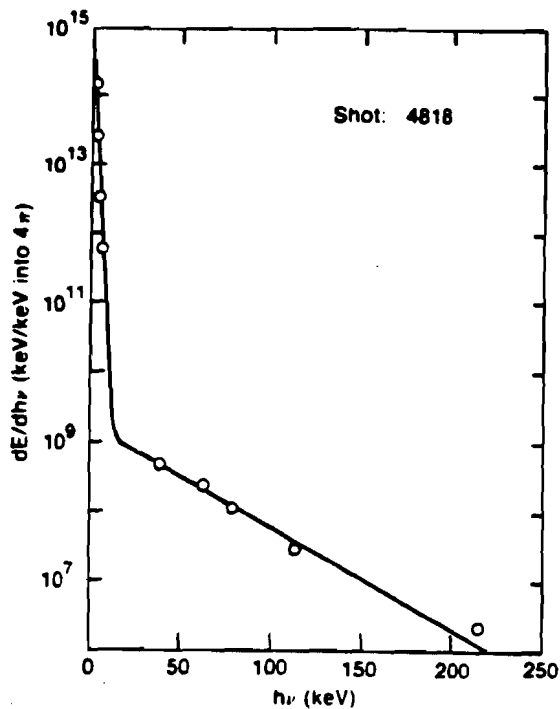
addition of additional detectors and optimized filter selection were made. During this period much was learned about optimizing the detector system through the choice of filters and filter thickness. This is covered in detail in Appendix E.

The results of the last series of $0.35 \mu\text{m}$ GDL experiments are shown in Table V-2 and the fits to the data obtained on several of these shots are shown plotted in figures V-7(a-c). Note that results obtained with both 0.5 and 1 ns pulse lengths are shown. Although in this data there appears to be a slight pulse length dependence, previously obtained results indicate that this effect is probably due to an uncertainty in the intensity. Slight changes in the divergence of the laser beam occurring between series of shots resulted in slight shifts in laser focal position and the resulting shift in intensity calibration.

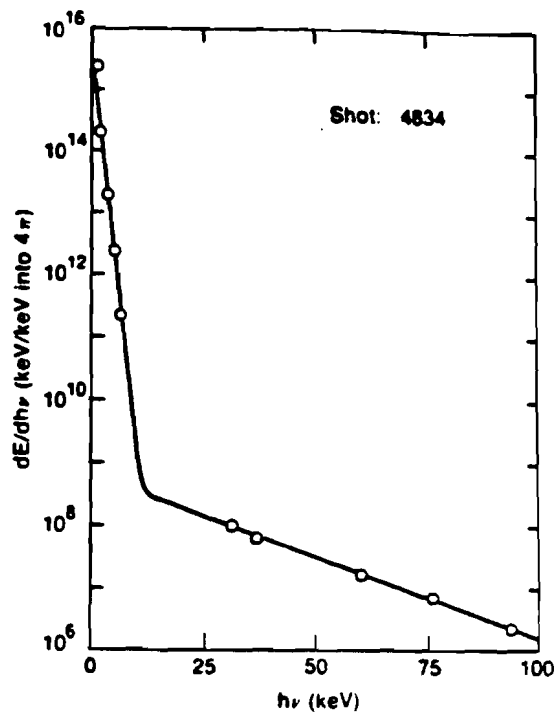
A limited number of experiments were performed in planar geometry at $1.05 \mu\text{m}$ on the GDL system by removing the frequency conversion crystals. These results are given in Table V-3. The high variability in these results probably results from the fact that when GDL is operated at $1.05 \mu\text{m}$ there is no laser prepulse suppression.

TABLE V-2. GDL 0.35 μm EXPERIMENTS SUMMARY

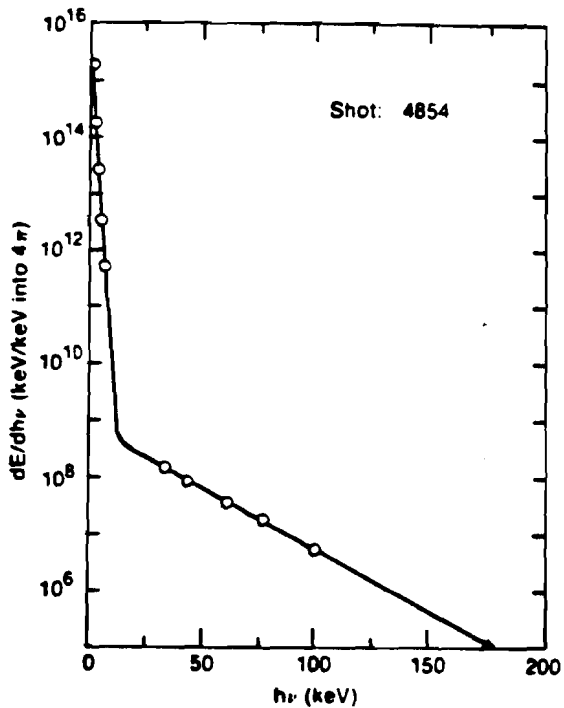
	Shot	Energy (Joules)	Intensity (W/cm^2)	Focus (mm)	Pulse Length (ps)	T_C (keV)	N_C (keV/keV)	T_{SH} (keV)	N_{SH} (keV/keV)
1	4816	37.7	1.11E+15	1.5	450	0.9	2.2E+15	28.7	1.2E+09
2	4817	37.4	1.10E+15	1.5	450	0.9	2.2E+15	24.2	2.5E+09
3	4818	38.6	1.13E+15	1.5	450	0.9	2.1E+15	29.5	1.7E+09
4	4819	38.4	1.13E+15	1.5	450	0.9	2.1E+15	25.7	2.3E+09
5	4820	38.9	1.14E+15	1.5	450	0.9	2.2E+15	31.8	1.5E+09
6	4821	36.3	1.07E+15	1.5	450	0.9	2.1E+15	23.1	2.9E+09
7	4822	38.9	1.14E+15	1.5	450	0.9	2.1E+15	24.8	2.5E+09
8	4823	39.9	3.84E+14	3.5	450	0.8	2.7E+15	19.3	1.2E+09
9	4824	40.4	1.57E+14	5.5	450	0.7	5.1E+15	18.4	2.8E+08
10	4833	38.4	5.07E+14	1.5	1000	0.7	5.5E+15	15.5	9.1E+08
11	4834	36.0	4.75E+14	1.5	1000	0.7	5.6E+15	16.6	6.6E+08
12	4839	36.3	1.57E+14	3.5	1000	0.6	9.5E+15	19.7	3.0E+07
13	4845	37.4	4.94E+14	1.5	1000	0.7	5.1E+15	20.2	6.0E+08
14	4848	34.1	1.48E+14	3.5	1000	0.6	9.9E+15	17.5	6.0E+07
15	4849	38.0	1.65E+14	3.5	1000	0.6	9.3E+15	13.7	1.6E+08
16	4854	36.3	3.49E+14	3.5	450	0.8	3.5E+15	20.1	8.1E+08
17	4855	45.2	4.35E+14	3.5	450	0.9	2.6E+15	25.0	1.4E+09
18	4856	41.1	1.60E+14	5.5	450	0.7	5.2E+15	19.2	2.5E+08
19	4863	40.1	1.18E+15	1.5	450	0.9	2.4E+15	30.7	1.2E+09
20	4866	38.2	1.12E+15	1.5	450	0.9	2.2E+15	27.1	2.5E+09



(a)



(b)



(c)

Figure V-7. Fits to data from several of the 0.35 μm GDL shots. Shot parameters may be found in Table V-2.

TABLE V-3. GDL 1.05 μm EXPERIMENTS SUMMARY

Shot	Energy (Joules)	Intensity (W/cm^2)	Focus (mm)	Pulse Length (ps)	T_C (keV)	N_C (keV/keV)	T_H (keV)	N_H (keV/keV)	T_{SH} (keV)	N_{SH} (keV/keV)	
1	5295	44.9	4.70E+13	7.0	1000	0.5	1.8E+16	2.8	3.3E+11	20.7	7.1E+07
2	5296	47.1	9.65E+13	5.0	1000	0.4	2.0E+16	2.6	5.6E+11	19.3	3.8E+08
3	5297	50.1	1.03E+14	5.0	1000	0.4	2.0E+16	3.2	3.5E+11	37.0	3.7E+07
4	5298	46.4	1.49E+14	4.0	1000	0.5	1.1E+16	3.5	3.0E+11	40.3	5.1E+07
5	5299	48.6	2.77E+14	3.0	1000	0.5	9.9E+15	3.4	3.9E+11	26.3	2.7E+08
6	5300	49.1	4.90E+14	2.0	1000	0.5	6.9E+15	3.6	3.0E+11	27.3	1.8E+08
7	5302	48.2	7.48E+14	1.0	1000	0.5	4.3E+15	3.4	3.1E+11	40.7	8.4E+07
8	5304	48.9	9.02E+14	0.0	1000	0.5	3.1E+15	4.0	1.9E+11	116.7	6.9E+06

B. OMEGA EXPERIMENTS

The OMEGA laser system is a 24 beam Nd-glass laser. It has been described in detail by Bunkenberg et al..³³ For these experiments the 24 beams were focused tangentially, eight target radii behind target center, to provide a high degree of illumination uniformity. The targets used were solid plastic (CH) spheres. The intensity on target was varied by changing the incident laser energy and the target diameter; targets of 200, 400 and 600 μm nominal diameter were used. The laser pulse length was 0.9 ns. Energy on target ranged from 300 to 1900 Joules.

The PIN detectors were mounted inside the target chamber, 35 inches from the target. The design of the detector array was similar to that used for the GDL experiments and illustrated in figure V-2a. The diodes were Quantrad model 025-PIN-250, having a nominal 25 mm^2 area with dead and active layer thicknesses specified at 0.75 and 250 μm respectively. The filtering used is shown in Table V-4.

Three of the NEI 6/1A-1.5/1HG 1 mm thick NaI scintillator detectors used in the GDL experiments were again used for these experiments. A Harshaw model 5SHB1M detector consisting of a 1 mm thick by 1.25 inch diameter NaI crystal integrally mounted to an RCA model 6199 photomultiplier was also used. These 1 mm thick NaI detectors were mounted in

TABLE V-4. OMEGA K-EDGE FILTERED DETECTOR SYSTEM PARAMETERS

Filter Material	Filter Thickness	K-edge (keV)	Detector Material	Detector Thickness	Detector Type
Cl (Saran)	50 μ m	2.8	Si	250 μ m	PIN
Sc	28	4.5	Si	250	PIN
Fe	25	7.1	Si	250	PIN
Ni	20	8.3	Si	250	PIN
Zn	47	9.7	Si	250	PIN
Y	253	17.0	Si	250	PIN
Mo	113	20.0	Si	250	PIN
Ag	136	25.5	Si	250	PIN
Ag	254	25.5	Si	250	PIN
Sn	250	29.2	NaI	1 mm	PMT
Ta	507	67.4	NaI	1	PMT
Pb	1.0 mm	88.0	NaI	1	PMT
Pb	2.5	88.0	NaI	50	PMT
Pb	5.7	88.0	NaI	50	PMT

24 inch long cylindrical lead collimators constructed of 1/8 inch lead sheet wrapped to a total wall thickness of 5/8 inch. The collimators were mounted to guide rails suspended from the target chamber and surrounding structures. This permitted the distance of the detectors to the target to be easily changed while maintaining collimator pointing. The detectors viewed the target through 1 mm aluminum vacuum windows. The K-edge filters were mounted on the front of the collimators. Lead plugs with 1/2 inch diameter apertures could be placed in the collimators when necessary to prevent PMT saturation.

The 2 inch thick Harshaw 8S8/2 NaI detectors used for the GDL experiments were also used for these experiments. They were again lead shielded, but essentially uncollimated. These detectors were simply placed on the equatorial personnel platform and viewed the target through a 1/2 inch thick aluminum port.

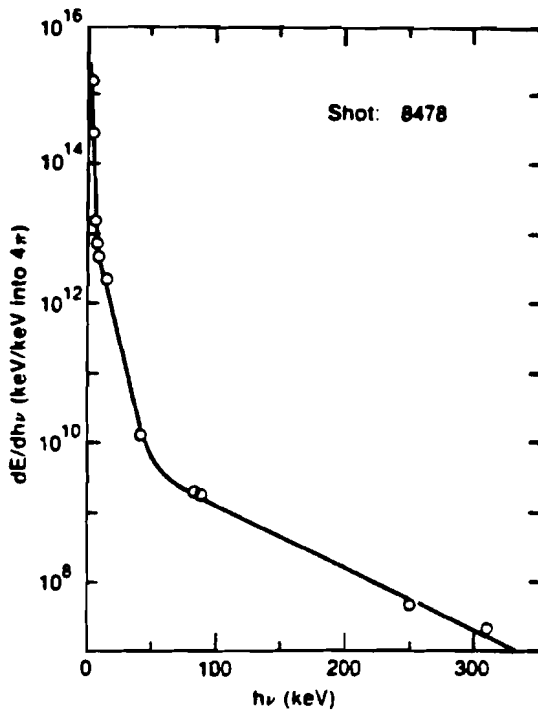
The signals from the detectors were acquired with essentially the same hardware and setup previously described for the GDL experiments and shown in figure V-6. The acquisition computer was in this case a DEC PDP-11/23. The acquisition software was written in FORTRAN and ran under the control of the OMEGA experimental operations control program and the RSX-11/M operating system. Signals were again monitored with oscilloscopes to check for noise or

detector saturation.

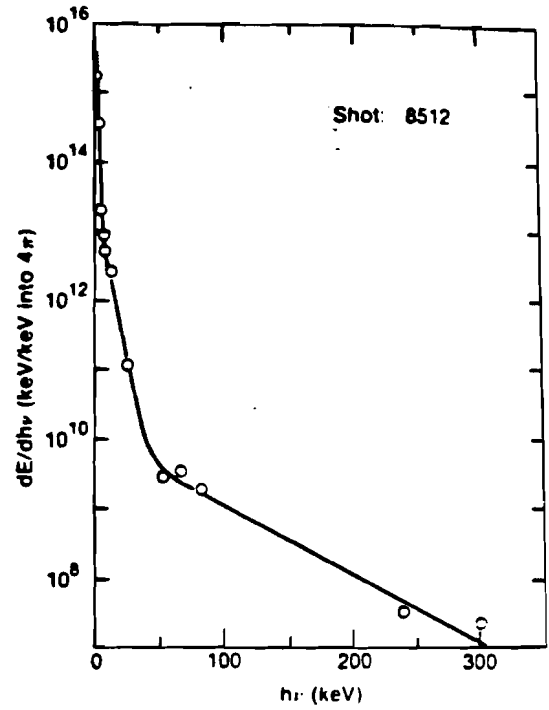
More than 120 shots were taken in this experimental series. Most of these were diagnostic shakedown shots which were utilized to set detector to target distance, check detector calibration and saturation levels, set gate timing, check for noise, etc.; 24 shots could be usefully reduced. The results of these are shown in Table V-5 and several fits are plotted in figures V-8(a-c).

TABLE V-5. OMEGA EXPERIMENTS SHOT SUMMARY

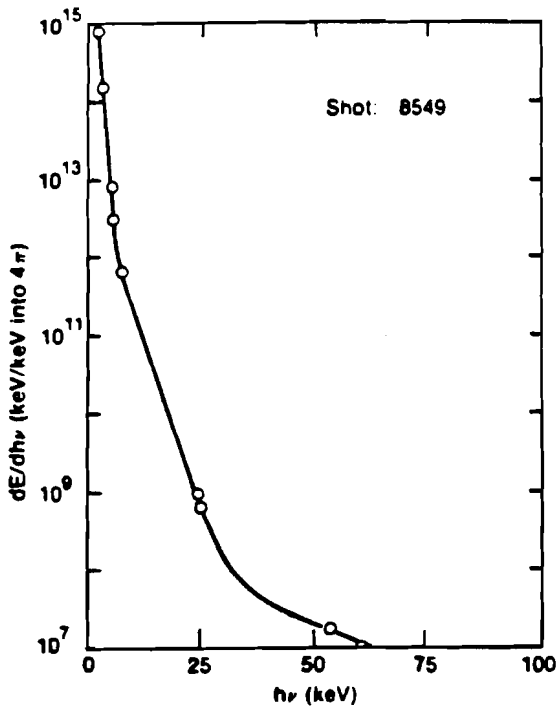
Shot	Target Radius (μm)	Incident Intensity (W/cm^2)	E_{inc} (Joules)	E_{abs} (Joules)	T_C (keV)	N_C (keV/keV)	T_H (keV)	N_H (keV/keV)	T_{SH} (keV)	N_{SH} (keV/keV)
1	8469	208	3.20E+14	1541.	0.6	5.81E+16	6.0	1.17E+13	51.9	1.78E+09
2	8470	208	3.39E+14	1668.	0.6	5.99E+16	6.3	1.23E+13	50.0	2.90E+09
3	8471	303	1.80E+14	1830.	0.6	1.45E+17	4.0	2.28E+13	53.4	6.03E+08
4	8477	97	1.76E+15	1780.	0.6	9.32E+16	5.4	2.11E+13	48.9	8.41E+09
5	8478	108	1.56E+15	1914.	0.6	9.88E+16	5.5	2.59E+13	48.6	9.99E+09
6	8479	303	1.56E+14	1476.	0.6	1.12E+17	3.6	1.74E+13	49.8	2.34E+08
7	8480	206	3.38E+14	1526.	0.6	6.71E+16	5.1	1.85E+13	48.6	2.61E+09
8	8482	103	1.50E+15	1616.	0.6	6.63E+16	5.1	2.07E+13	46.2	7.90E+09
9	8493	206	4.32E+14	1856.	0.6	8.43E+16	4.5	3.47E+13	41.2	1.18E+10
10	8494	191	5.06E+14	1877.	0.6	8.58E+16	4.6	3.51E+13	41.7	1.28E+10
11	8495	206	3.70E+14	1793.	0.6	7.68E+16	4.4	3.18E+13	43.1	5.65E+09
12	8496	206	4.24E+14	1936.	0.6	7.52E+16	4.7	3.15E+13	43.3	1.00E+10
13	8497	206	3.69E+14	1782.	0.6	7.27E+16	4.6	2.94E+13	42.0	8.00E+09
14	8508	211	4.15E+14	2048.	0.6	9.43E+16	4.7	3.78E+13	43.7	1.00E+10
15	8511	208	4.14E+14	2053.	0.6	9.90E+16	4.7	3.88E+13	43.7	1.06E+10
16	8512	211	4.17E+14	2056.	0.6	1.04E+17	4.6	3.81E+13	43.7	1.08E+10
17	8522	108	1.42E+15	1907.	0.6	5.72E+16	4.8	3.26E+13	46.0	1.11E+10
18	8527	211	2.86E+14	1389.	0.6	7.28E+16	4.0	2.52E+13	47.8	1.02E+09
19	8528	307	1.67E+14	1820.	0.6	1.06E+17	3.6	2.82E+13	49.3	3.05E+08
20	8529	301	1.83E+14	1845.	0.6	1.04E+17	3.8	2.71E+13	30.0	2.86E+09
21	8548	290	1.73E+14	1764.	0.6	1.13E+17	3.5	3.10E+13	26.4	4.51E+09
22	8549	307	9.61E+13	1038.	0.6	4.96E+16	2.6	1.10E+13	18.7	3.05E+08
23	8550	305	4.86E+13	661.	0.5	3.72E+16	2.2	4.15E+12	43.5	1.24E+06
24	8551	305	4.56E+13	499.	0.5	5.24E+16	1.9	1.17E+13		



(a)



(b)



(c)

Figure V-8. Fits to data from several of the 1.05 μm OMEGA shots. Shot parameters may be found in Table V-5.

CHAPTER VI
DISCUSSION

The data presented in Tables V-2 and V-5 has been plotted, along with relevant data from other sources, in figures VI-1 to VI-6. In a few cases, poorly determined data from low intensity shots has been omitted from the plots. Perhaps the most evident feature of the data, best illustrated by comparing the fits shown in figures V-7(a-c) and V-8(a-c), is that the 0.35 μm data can be fit using a two temperature model, while the 1.05 μm data require a three temperature model. The three temperatures observed at 1.05 μm will be referred to as cold, hot and super-hot. The super-hot component can be attributed to the production of very fast electrons by parametric instabilities occurring near $n_c/4$. The hot component corresponds to fast electron production by resonance absorption. This component is not observed in the 0.35 μm experiments.

In the following sections, the hot and super-hot components will be considered in detail. The cold component, produced by the overdense plasma, remains essentially constant in temperature over the measured intensity range and

will not be further mentioned. Because of their high variability, the planar GDL 1.05 μm results have not been plotted. Inspection of Tables V-3 and V-5 shows them to be in general agreement with the spherical OMEGA 1.05 μm results. This indicates, that for this measurement, geometrical effects are not important.

A. THE HOT SPECTRAL COMPONENT

The temperature of the hot component measured on the OMEGA 1.05 μm experiments is plotted as a function of incident intensity in figure VI-1a. The temperature scales with intensity approximately as $I^{1/3}$ except at the highest intensities. This is primarily a target expansion effect. Spatially resolved measurements of harmonic emission from the target³⁴ and numerical results obtained with the hydrodynamic code SAGE³⁵ indicate that the critical surface is located approximately 55 μm from the initial target surface at the peak of the laser pulse. This reduces the effective intensity by factors of 2.6, 1.6 and 1.4 for 200, 400 and 600 μm targets respectively. The data are replotted in figure VI-1b with this intensity correction. With this correction, an approximate $I^{1/3}$ scaling is observed throughout the measured range. The intensity corrected data is in good agreement with previous experimental work¹³ and scaling obtained from numerical simulation of resonance

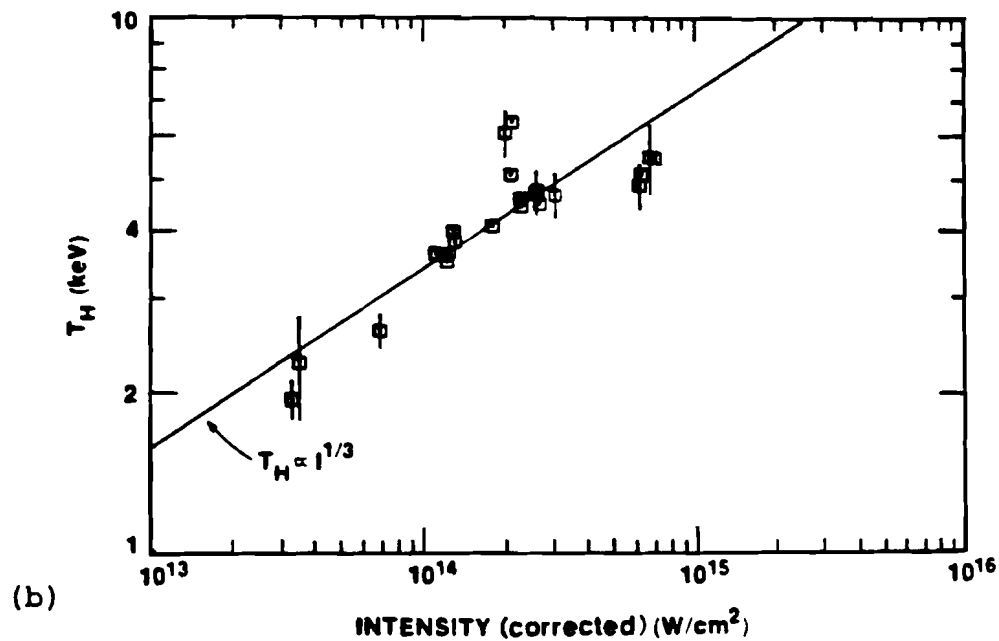
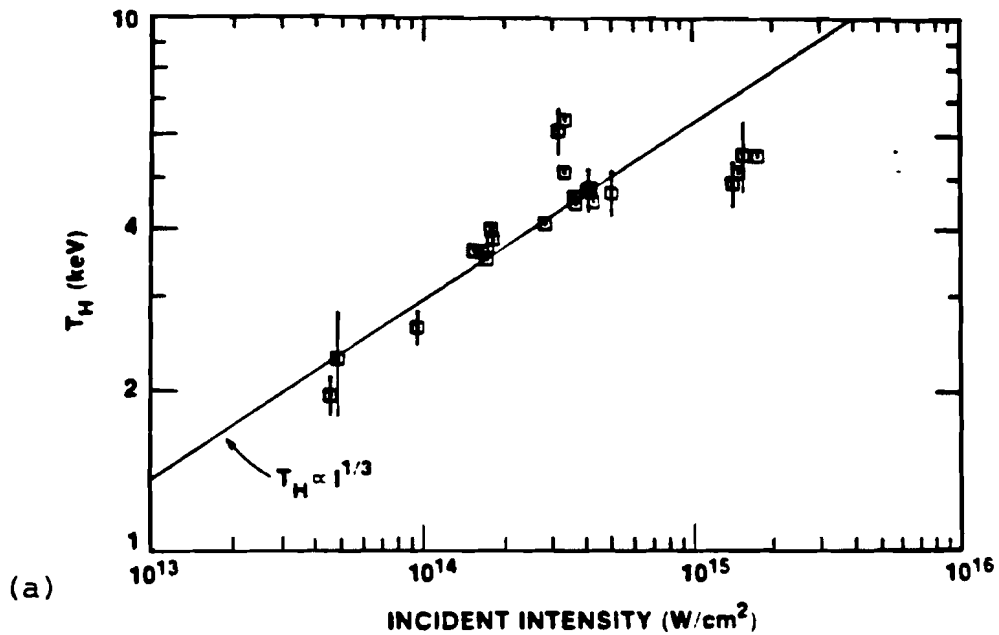


Figure VI-1. T_H at $1.05 \mu m$ as a function of nominal incident intensity (a) and as a function of intensity corrected for the excursion of the critical surface (b).

absorption.¹⁶

The energy in the hot electron component, as determined from N_H using Brueckner's model, relative to energy absorbed is shown in figure VI-2a along with the measured absorption of the incident laser. Again, the data is replotted in figure VI-2b with the intensity correction for target expansion. The energy in the hot electron component is somewhat higher than expected. For example, ref. 14 measures $E_H/E_{ABS} \approx 0.34$ at 10^{15} W/cm². For comparison, the hot electron fraction predicted by SAGE is also plotted, where in the calculation 15% of the energy reaching the critical surface was deposited in fast electrons. Clearly these points can be shifted by changing the fractional dump at critical; 15% represents a figure which provides reasonable agreement between the code and a wide variety of measurements made at LLE and elsewhere.

Considering the error bars on the measured E_H/E_{ABS} , the measured values are not unreasonable. Because the measured T_H is comparable to the coronal temperature, a possible source of bias is unresolved contributions to the spectrum from the coronal plasma. This would bias the measurement of T_H to slightly lower values. Recalling from chapter IV that T_H and N_H have a strong negative correlation, this would result in a measured E_H/E_{ABS} that was artificially high. Inspection of the outlying data points in figures VI-1 and

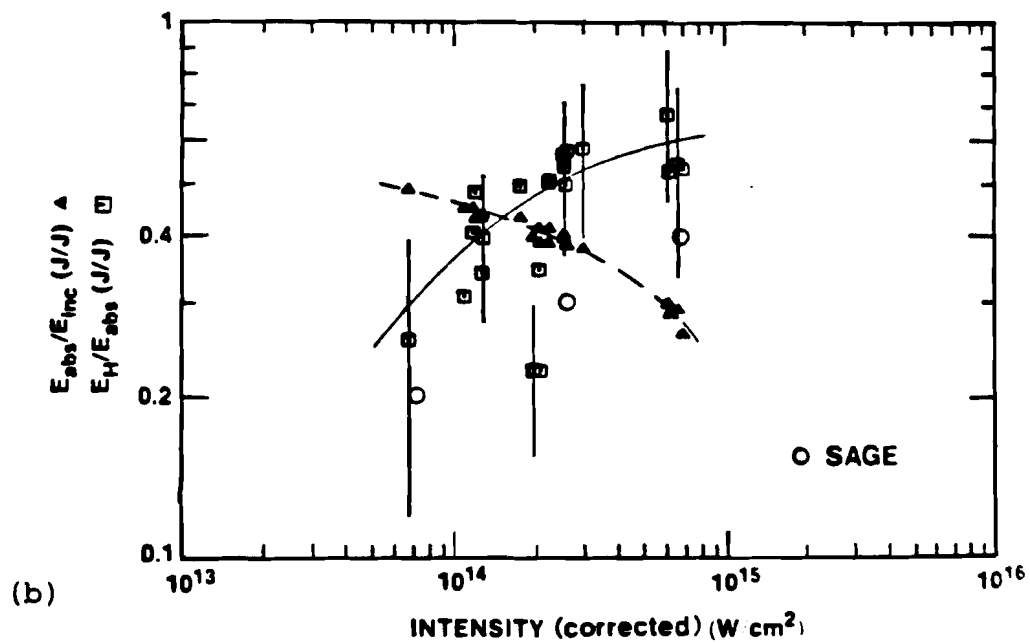
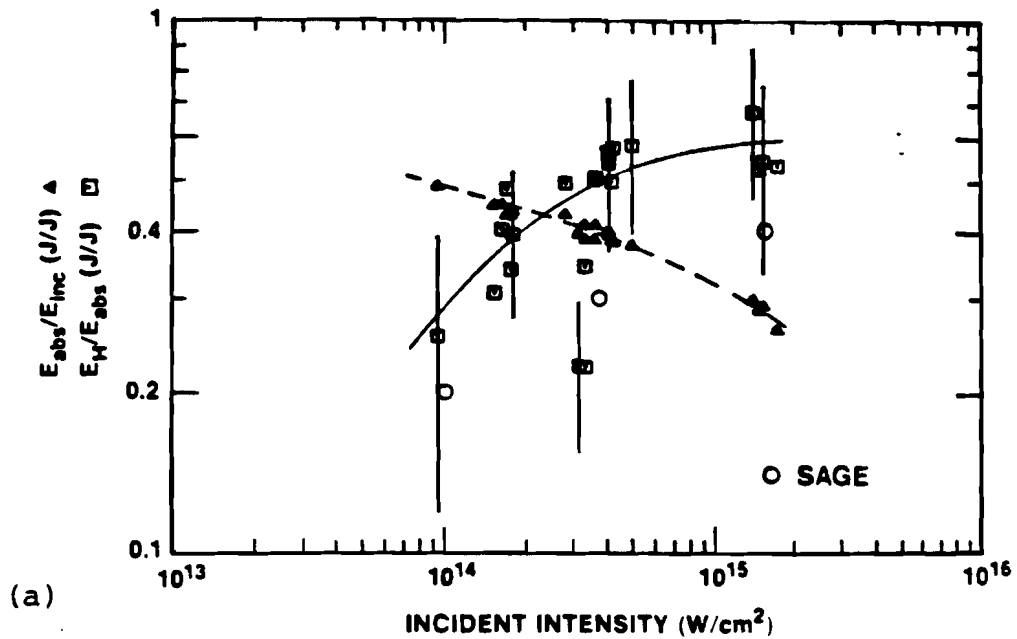


Figure VI-2. Fractional energy in hot electrons at $1.05 \mu m$ as a function of nominal incident intensity (a) and intensity corrected for the excursion of the critical surface (b). Also shown are the results of SAGE calculations for a 15% dump into fast electrons and the measured laser absorption.

VI-2 shows that a small change in the determination of T_H results in a significant change in E_H/E_{ABS} .

B. THE SUPER-HOT SPECTRAL COMPONENT

The temperature of the super-hot component measured on the 1.05 μm OMEGA experiments is shown in figure VI-3a. The data are replotted in figure VI-3b incorporating an intensity correction for target expansion. Since we attribute the super-hot component to quarter critical parametric instabilities, in this case the correction is for intensity at $n_c/4$, which is on the basis of harmonic measurements and SAGE calculations located approximately 120 μm from the initial target surface. When this correction is made the data spans such a limited intensity range and its scatter is so high, that it not possible to draw any conclusions on the temperature scaling with intensity.

In contrast, the 0.5 ns, 0.35 μm data obtained on the GDL experiments, figure VI-4, does indicate a slow $I^{0.2}$ scaling with intensity. It should be noted that the intensity on GDL is not well defined since the beam is not uniform. By convention, the intensity used when presenting GDL data is defined as 1.5 times the average intensity. This same intensity nonuniformity may distort the measured scaling of quantities which have a threshold behavior if

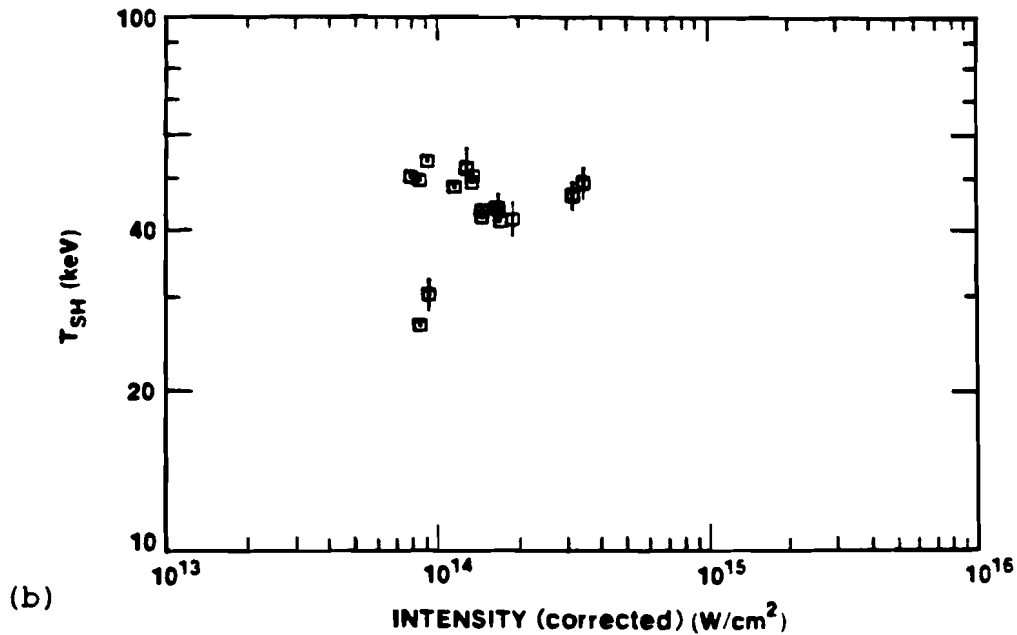
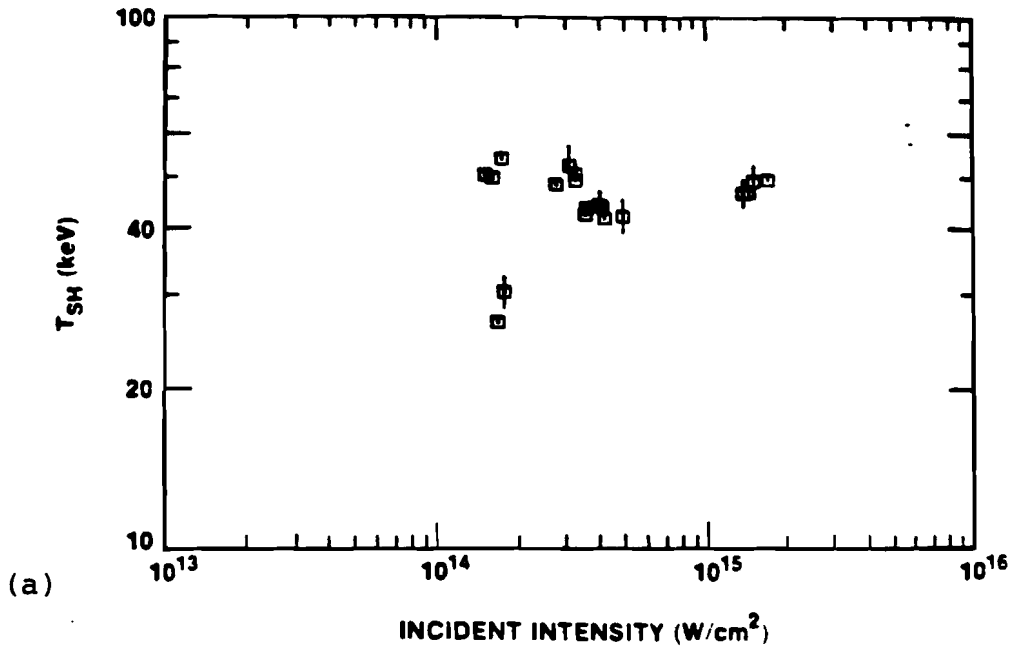
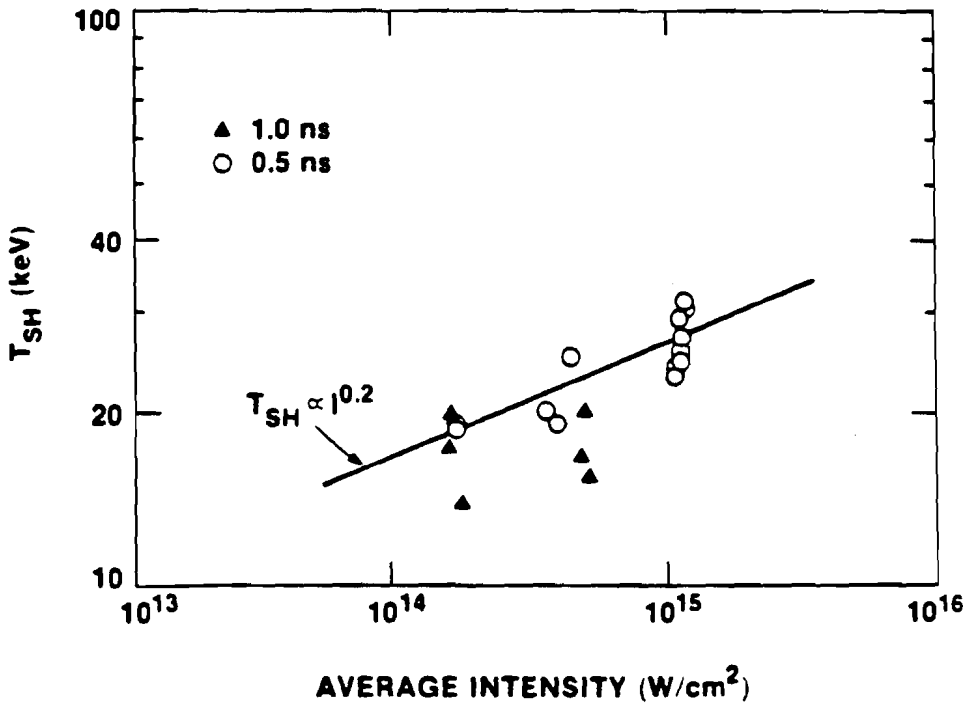


Figure VI-3. T_{SH} at $1.05 \mu m$ as a function of nominal incident intensity (a) and intensity corrected for the excursion of the quarter critical surface (b).

SUPER-HOT X-RAY TEMPERATURE (0.35 μm)



E2407

Figure VI-4. Super-hot temperature measured at 0.35 μm on GDL.

they are measured near threshold. In Appendix F, it is shown that if the beam nonuniformity is taken into consideration, the measured $I^{0.2}$ scaling may indicate an actual $I^{0.3}$ scaling. This would be in agreement with the predicted $(I\lambda^2)^{1/3}$ scaling predicted in ref. 20.

The above scaling law also indicates that there should be a scaling of T_{SH} as $\lambda^{2/3}$. Because of the problems noted above, it can really only be noted that T_{SH} does decrease with wavelength by a factor of about the right order.

The relative energy in the super-hot electron component is shown in figure VI-5a and corrected for intensity in figure VI-5b. A clear threshold behavior is seen with E_{SH}/E_{INC} decreasing rapidly below about 2×10^{14} W/cm² and saturating above this intensity. The dashed curve in figures VI-5a shows the relative energy in the $3/2\omega_0$ signal from the target.³⁶ This is a signature of plasma wave producing instabilities, e.g. Raman and $2\omega_p$, at $n_c/4$. A reasonably strong correlation between the $3/2\omega_0$ signal and electron energy can be observed.

The relative energy in the super-hot component measured in the 0.35 μ m GDL experiments is shown in figure VI-6. Again a rise and saturation behavior is evident. Also plotted is the $\omega_0/2$ signal produced by $2\omega_p$.⁶ Again the x-ray signal and $\omega_0/2$ signal track remarkably closely.

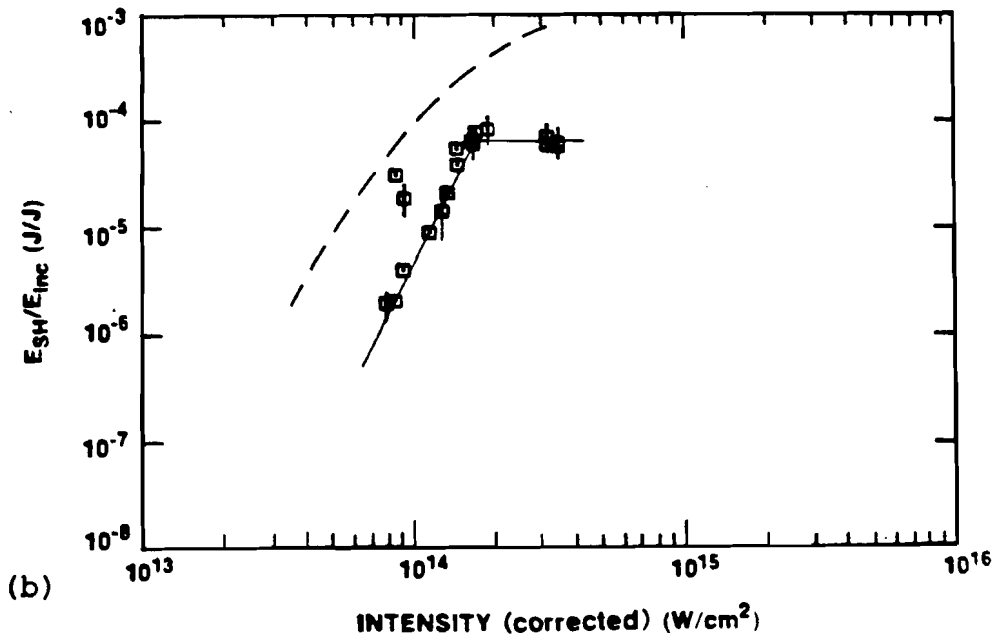
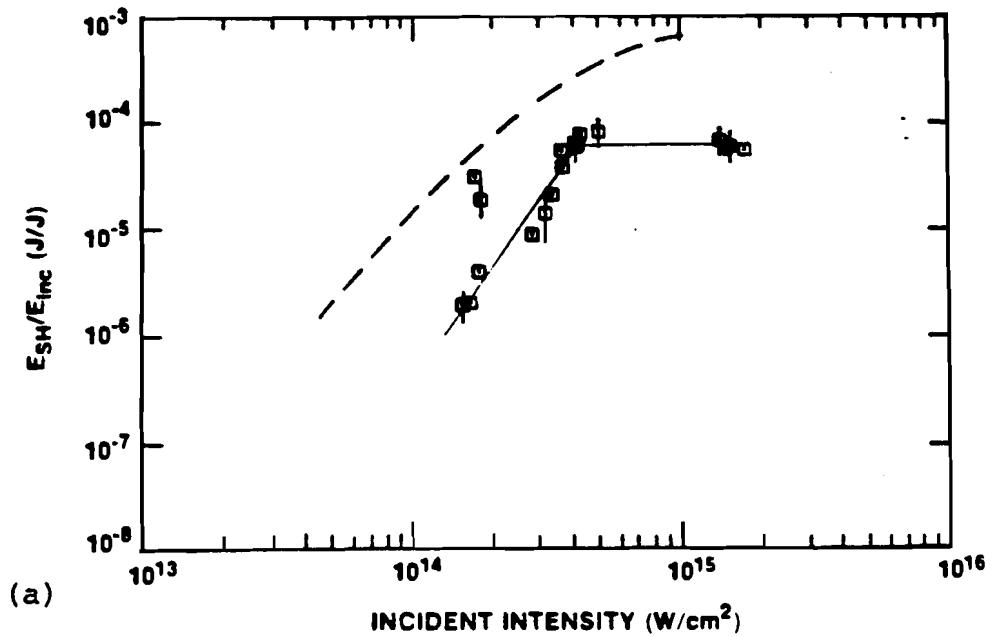
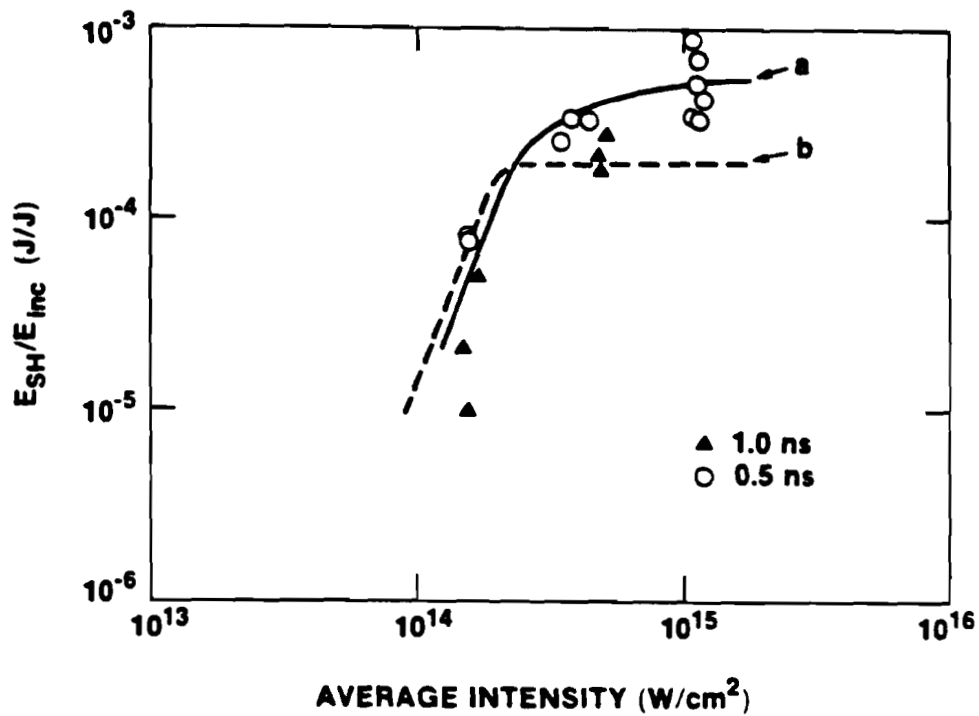


Figure VI-5. Relative energy in super-hot electrons at $1.05 \mu m$ as a function of nominal incident intensity (a) and corrected for the excursion of quarter critical (b). Also shown is the $3/2\omega_0$ signal (dashed curve) (from ref. 36).

RELATIVE SUPER-HOT ELECTRON ENERGY (0.35 μm)



E2390

Figure VI-6. Relative energy in super-hot electrons at 0.35 μm on GDL. Curve (a) is a fit to the 0.5 ns data. The dashed curve (b) is the $\omega_0/2$ light signal from the target (from ref. 6).

Figure VI-7 shows the scaling of E_{SH}/E_{INC} obtained from an early, more extensive data set at $0.35 \mu\text{m}$ on GDL. Because of less than optimal filtering, the absolute magnitude of the data is less well determined than the data presented in figure VI-6. However, it better illustrates the detailed scaling of E_{SH}/E_{INC} with intensity. Also shown in figure VI-7 is the relative signal from the Raman instability (curve a) and the $2\omega_p$ instability (curve b) obtained in ref. 6. Since no increase in the x-ray signal is observed to occur when the Raman instability is observed to occur, we conclude that the super-hot component is being produced primarily by the $2\omega_p$ instability. Because the $\omega_0/2$ light is produced indirectly by $2\omega_p$, while it is produced directly by Raman, this observation may simply indicate that Raman is occurring at lower amplitudes, rather than that Raman is less effective than $2\omega_p$ at producing fast electrons.

As noted previously, the GDL data are plotted as a function of an average intensity. The threshold intensity should be evaluated in terms of the peak beam intensity, which is a factor of approximately 3 higher than the plotted intensity. Thus a given value of E_{SH}/E_{INC} occurs at an intensity approximately a factor of 3 higher at $0.35 \mu\text{m}$ than at $1.05 \mu\text{m}$.

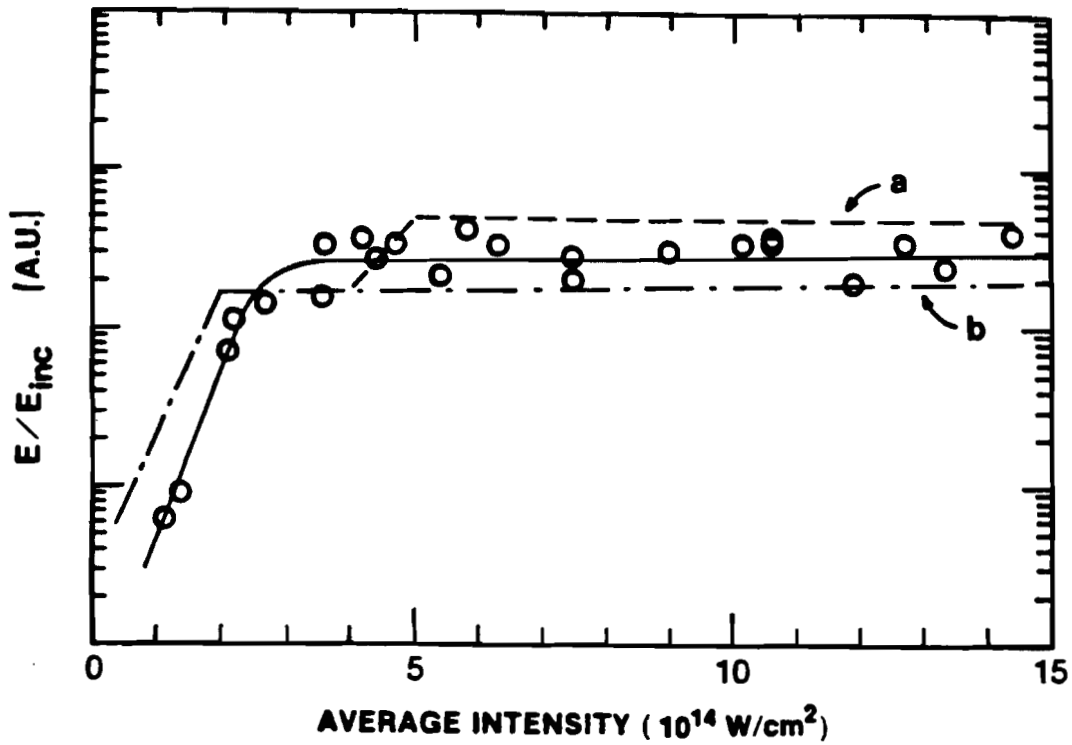


Figure VI-7. E_{SH}/E_{INC} from an earlier set of experiments at $0.35 \mu\text{m}$ on GDL. Also shown is the relative $2\omega_p$ signal (curve b) and Raman signal (curve a) (from ref. 6).

C. CONCLUSIONS

The results obtained here, as well as the high measured absorptions and low preheat at $0.35 \mu\text{m}^{2,37}$, confirm that the absorption of $0.35 \mu\text{m}$ laser light is dominated by inverse bremsstrahlung. The more interesting feature of the measurements is the presence of the super-hot electron component at both laser wavelengths. Because the x-ray signal is correlated with the observation of $\omega_0/2$ light from the $0.35 \mu\text{m}$ plasmas and $3\omega_0/2$ light from the $1.05 \mu\text{m}$ plasmas and because there was no increase in x-ray intensity when the Raman instability was observed to occur, we believe that the $2\omega_p$ instability is primarily responsible for the super-hot electron distribution.

Regardless of the source of the super-hot component, it is interesting to note from a laser fusion perspective that the two driver wavelengths measured here are comparable in their production of super-hot electrons. While the low level of super-hot electron production observed in these experiments would not prove an obstacle to efficient target compression, production of fast electrons from quarter critical instabilities will need to be monitored as it becomes possible to perform experiments on larger targets more similar to those required for laser fusion reactors.

APPENDIX A
PMT CALIBRATION

The PMT scintillators were calibrated using single photons of known energy provided by nuclear sources. To the extent that the photomultiplier is linear over the required range, this also provides the large signal or multiple photon calibration. When properly operated, photomultipliers are in fact highly linear devices. Their dynamic range is limited at high signal levels by saturation of either the input (photo-cathode) or output (anode). If anode saturation occurs first, as was the case with the tubes used here, their dynamic range may be extended by varying the tube gain, which can be done by changing the applied high voltage. In addition to single photon calibration, additional cross calibration was done at operating signal levels to ensure that the tubes were not saturated.

The calibration setup shown schematically in figure A-1. The LeCroy 2249W integrating A/D, CAMAC, LSI-11 and software were used together as a multichannel analyzer. A LeCroy 321B quad discriminator was used to generate a suitable gate for the 2249W and a variable delay ensured that

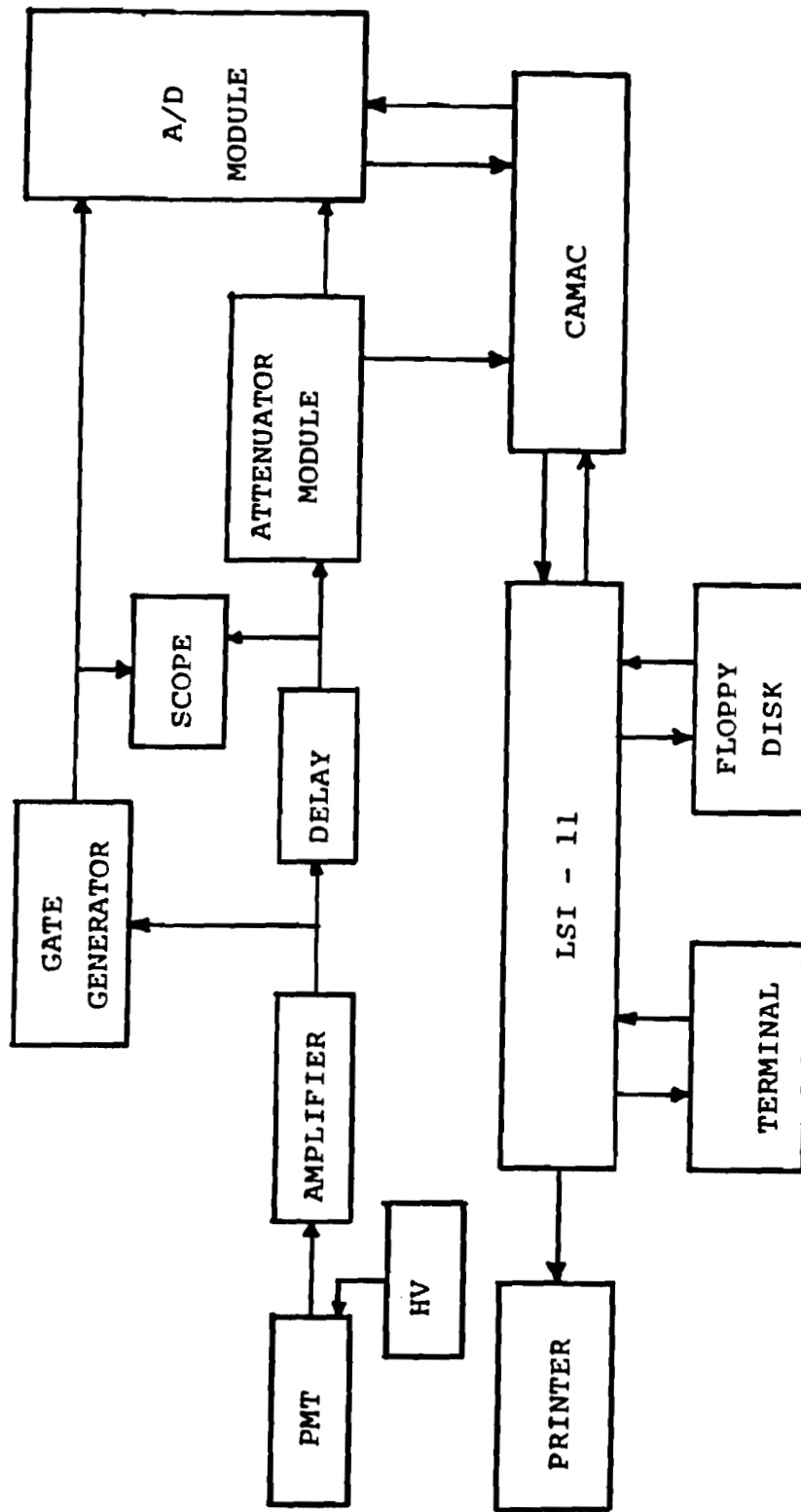


Figure A-1. Configuration used for NaI-PMT detector calibration. The A/D module, CAMAC and LSI-11 were used together as an MCA.

the signal reached the 2249W at the center of the gate interval. A LeCroy 133B dual linear amplifier was used to obtain suitable signal levels into the 2249W. An oscilloscope was utilized to verify that the system was functioning properly.

The 1 mm thick NEI and Harshaw detectors were calibrated using an Americium 241 source which emits 59.6 keV photons. The 2 inch thick Harshaw detectors were calibrated using a Cobalt 60 source which emits photons at 1.17 and 1.33 MeV.

For a typical calibration, 1000 events would be collected by the system. Since the 2000 bin resolution of the 2249W was not required, counts were generally combined over a 10 to 20 bin range and then displayed on a printer. An example of the resulting output is reproduced in figure A-2. The two photoelectric peaks from the 1.17 and 1.33 MeV photons are clearly visible. The calibration constant for a particular detector and applied high voltage was determined by dividing the charge obtained per photon at the center of the photoelectric peak by the energy of the corresponding incident photons.

Each detector was calibrated at several values of applied high voltage. Since the gain of a photomultiplier³⁸ is proportional to V^a the results were fit using a least square fit to CxV^a . This permitted the gain of the detec-

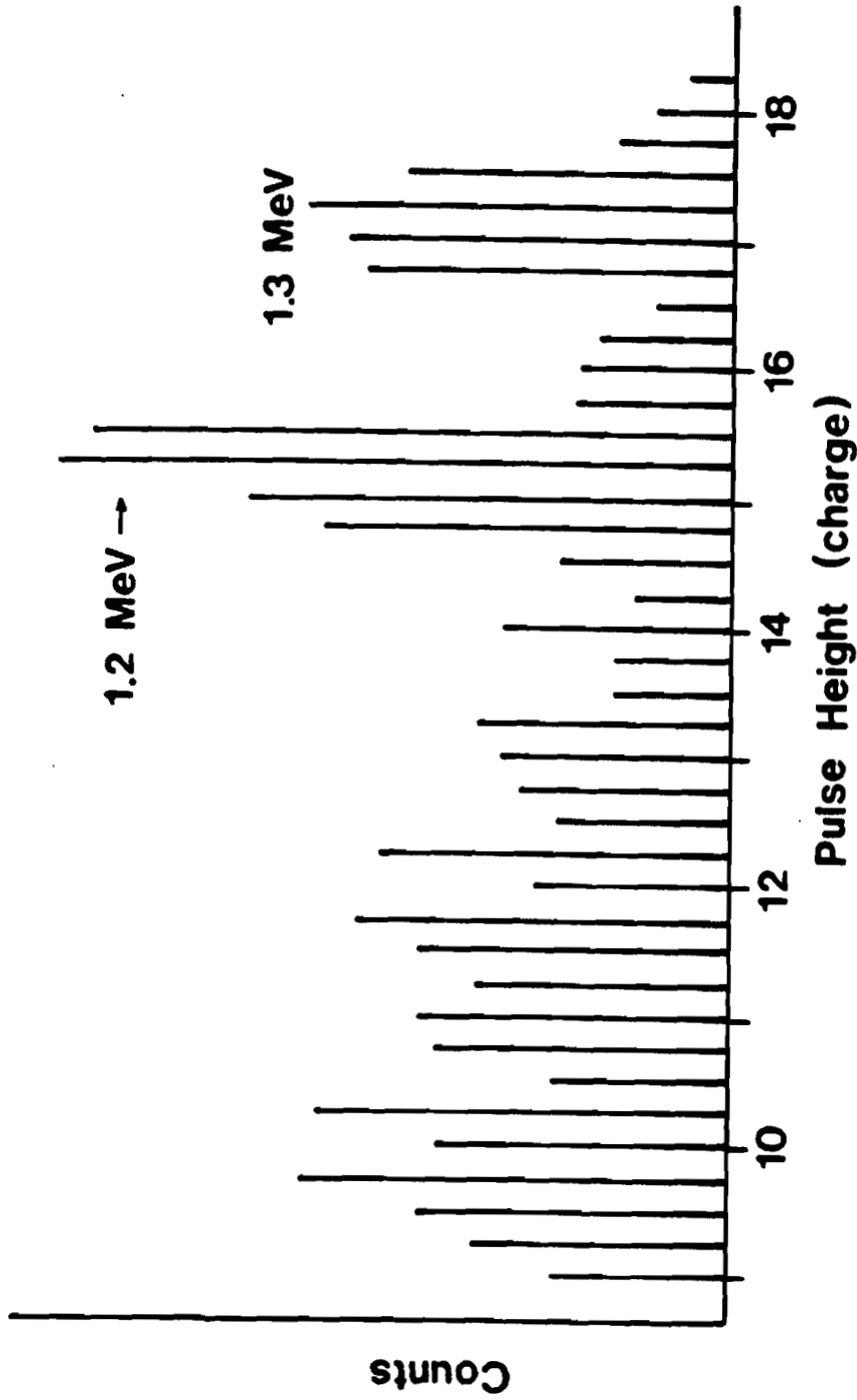


Figure A-2. MCA output obtained with the setup shown in figure A-1. The detector was 50 mm thick NaI and the source was Co^{60} . The two photoelectric absorption peaks are clearly visible.

tors to be conveniently varied to suit the signal levels encountered during experiments by varying the applied high voltage, while retaining calibration. The detectors were recalibrated several times during the course of the experiments. Calibrations were found repeatable to within about 10%.

The detectors were additionally checked at operating signal levels by filtering them identically and exposing them to target shots. It was found that their relative calibration held to within about $\pm 30\%$ of the small signal value. For this reason, the calibration of each tube is considered accurate to $\pm 30\%$. It was also verified, by changing the detector to target distance of some detectors while leaving others fixed, that the detectors were operating in a linear range.

APPENDIX B
PIN CALIBRATION

Equation (III-3) provides the sensitivity of a PIN diode assuming the thicknesses of the dead and active layers of the diodes are known. These figures are normally supplied by the manufacturer. Using diodes of identical type and manufacture to the ones used in these experiments, Corallo et al.²⁷ found there to be considerable variation in the thickness of these layers, as determined by measuring the diode sensitivity, from the manufacturer's specification. In particular, nominal 125 μm active layer diodes had active layers ranging from 110 to 170 μm and nominal 250 μm diodes ranged from 235 to 295 μm . Variations from nominal were also found in the dead layer thickness, but in these experiments this has virtually no effect on diode sensitivity.

The detectors most sensitive to variations in active layer thickness are the higher energy ones. In order to estimate the effect of active layer thickness on expected signal, the expected signal can be calculated for a high Z filtered diode at infinite temperature, which is the worst

case. This was done for a yttrium filtered diode over the range of thicknesses measured in ref. 1. It was found that over this range a 1% variation in thickness corresponds to a 1% change in expected signal. Thus, the 125 μm diodes can be expected to be accurate to about -12, +36% worst case and the 250 μm diodes -6, +18% worst case.

APPENDIX C
FLUORESCENT ESCAPE

Even with a semi-infinite detector, a certain fraction of the fluorescence photons produced by incident x-rays will escape the detector. This is significant only if the energy of the incident photon is just above an absorption edge energy of the detector. In this case the incident x-ray has a high probability of being absorbed close enough to the surface that the fluorescent photon is likely to escape. An expression for the fraction of fluorescent photons which escape the detector was given in equation (III-2). This is obtained as follows.

Consider the geometry shown in figure C-1. An incident x-ray of energy $h\nu$ undergoes photoelectric absorption a distance X from the surface of the detector. A fluorescent photon emitted at an angle ϕ then must travel a distance $R = X/\cos(\phi)$ to escape the detector. The photon flux at X is:

$$I_0 e^{-\sigma_T(h\nu)X},$$

where I_0 is the flux at the surface of the detector and σ_T is the total scattering cross section.

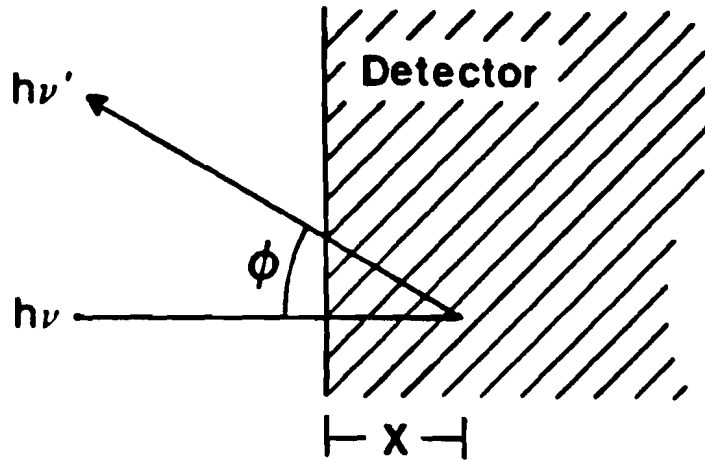


Figure C-1. Geometry for fluorescent photon escape.

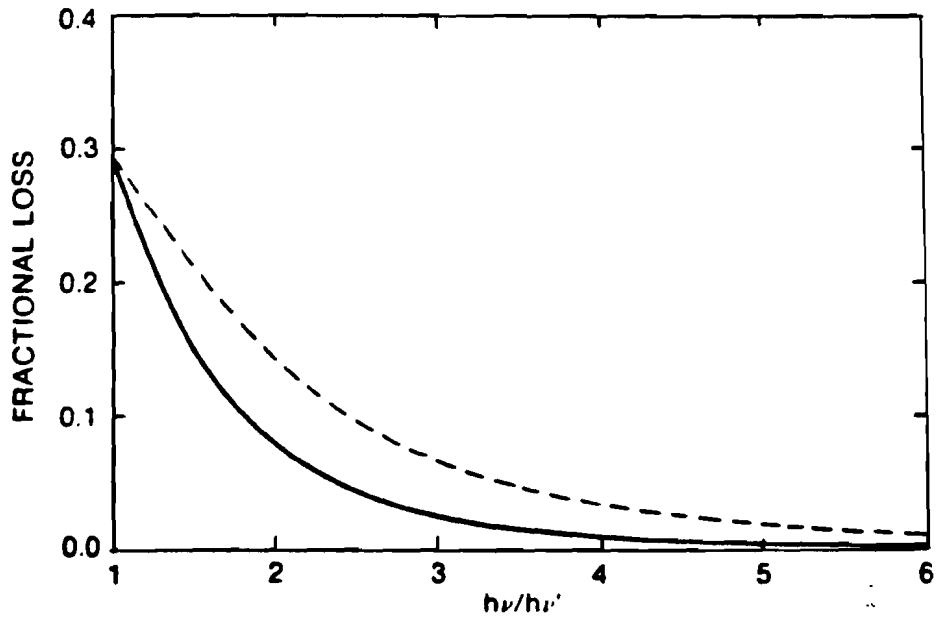


Figure C-2. Fractional loss of fluorescent photons (dashed curve) and energy (solid curve) from a semi-infinite NaI detector.

The number of fluorescent photons produced in the detector in the layer between X and $X+dX$ is:

$$I_0 e^{-\sigma_T(h\nu)X} \sigma_P(h\nu) dX$$

so the fluorescent flux observed outside the detector at the angle ϕ is:

$$I_0 e^{-\sigma_T(h\nu)X} \sigma_P(h\nu) e^{-\sigma_T(h\nu')R} dX \frac{d\Omega}{4\pi} \quad (1)$$

where σ_P is the photoelectric cross section and $h\nu'$ is the energy of the fluorescent photon.

To obtain the total number of fluorescent photons which are produced and escape (1) is integrated over the thickness of the detector and the full solid angle. For the semi-infinite detector this is:

$$\begin{aligned} I &= \frac{I_0}{4\pi} \sigma_P(h\nu) \int_0^{\pi/2} \int_0^{2\pi} \int_0^{\infty} e^{-x(\sigma_T(h\nu) + \sigma_T(h\nu')/\cos\phi)} dx d\theta \sin\phi d\phi \\ &= \frac{I_0 \sigma_P(h\nu)}{2} \int_0^1 \frac{\cos\phi}{(\sigma_T(h\nu) \cos\phi + \sigma_T(h\nu'))} d\cos\phi \\ &= \frac{I_0}{2} \frac{\sigma_P(h\nu)}{\sigma_T(h\nu)} \left(1 - \frac{\sigma_T(h\nu')}{\sigma_T(h\nu)} \ln \left(1 + \frac{\sigma_T(h\nu)}{\sigma_T(h\nu')} \right) \right) \end{aligned} \quad (2)$$

This last expression is just equation (III-2).

Equation (2) provides the number of fluorescent photons which escape the detector. Because these photons have energy $h\nu'$ while the incident photons have energy $h\nu$, the energy which escapes the detector is reduced by the factor $h\nu'/h\nu$.

Equation (2) and $(2) \times h\nu'/h\nu$ are plotted in figure C-2 for the case of an NaI detector at the K-edge of iodine.

APPENDIX D
FILTER FOIL FLUORESCENCE

When an x-ray is photoelectrically absorbed in a filter foil a fluorescence photon will generally be produced. If the foil is thin there is some probability that it may escape the foil and impact the detector. In these experiments, the filter foils were generally mounted far from the detector, so the fractional solid angle of the detector with respect to the foil was small. This minimized the fluorescence contribution to the total detector signal. Because it was impractical to collimate them, the lead filter foils for the 2 inch Harshaw detectors were mounted only about 1 inch from the front of the crystals. As is shown below, fluorescence in this case was minimized simply because the foils were thick enough to absorb most of their own fluorescence.

Consider the geometry shown in figure D-1. A photon of energy $h\nu$ is photoelectrically absorbed a distance Y into a foil of total thickness X . The resultant fluorescent photon escapes the rear of the foil at an angle θ as shown. The photon flux at Y is:

$$I_0 e^{-\alpha_T(h\nu)Y}$$

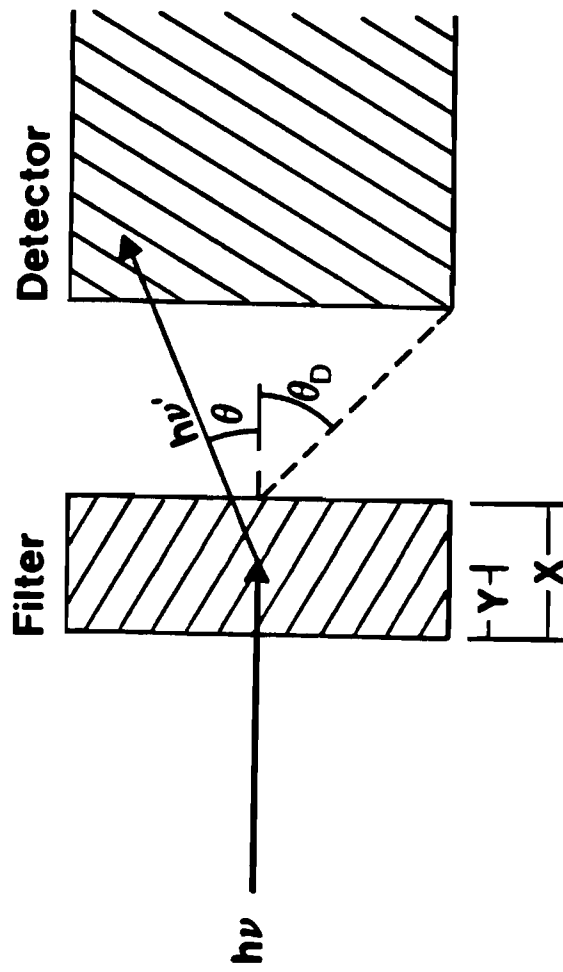


Figure D-1. Geometry for filter foil fluorescence.

where I_0 is the flux at the surface of the detector and σ_T is the total scattering cross section.

The number of fluorescent photons produced in the foil in the layer between Y and $Y+dY$ is:

$$I_0 e^{-\sigma_T(h\nu)Y} \sigma_P(h\nu) dY$$

so the fluorescent flux observed outside the foil at the angle θ is:

$$I_\theta = e^{-\sigma_T(h\nu)Y} e^{-\sigma_T(h\nu')(X-Y)/\cos\theta} \sigma_P(h\nu) dY \frac{d\Omega}{4\pi} \quad (1)$$

where σ_P is the photoelectric cross section and $h\nu'$ is the energy of the fluorescent photon.

To obtain the total number of fluorescent photons which reach the detector (1) is integrated over the thickness of the foil and the solid angle of the detector. Hence:

$$I = \frac{I_0}{4\pi} \sigma_P(h\nu) \int^{\Omega_D} e^{-\sigma_T(h\nu')X/\cos\theta} \int_0^X e^{-Y(\sigma_T(h\nu) - \sigma_T(h\nu')/\cos\theta)} dY d\Omega \quad (2)$$

$$= \frac{I_0}{4\pi} \sigma_P(h\nu) \int^{\Omega_D} \frac{e^{-\sigma_T(h\nu')X/\cos\theta} - e^{-X\sigma_T(h\nu)}}{\sigma_T(h\nu) - \sigma_T(h\nu')/\cos\theta} d\Omega \quad (3)$$

To obtain the energy transferred to the detector, (3) must be multiplied by $h\nu'/h\nu$.

The fluorescent contribution to detector signal can be estimated from (3) as follows. An upper bound to (3) is obtained by taking $\theta = 0$ where it appears in the integrand. Then (3) becomes:

$$I_E(h\nu) = (\Omega_D/4\pi) I_0 F(h\nu) (h\nu'/h\nu) \quad (4)$$

where we define $F(h\nu)$ as:

$$F(h\nu) = \sigma_P(h\nu) \frac{e^{-X\sigma_T(h\nu')} e^{-X\sigma_T(h\nu)}}{\sigma_T(h\nu) - \sigma_T(h\nu')} \quad (5)$$

and the factor $h\nu'/h\nu$ has been incorporated to account for the fixed energy of the fluorescent photon. $F(h\nu)$ and $F(h\nu) (h\nu'/h\nu)$ have been plotted in figure D-2 for the case of a 2.54 mm lead foil.

The fluorescent signal produced in the detector is given by:

$$S_F = \frac{\Omega_D}{4\pi} \int_{h\nu}^{\infty} \frac{dE}{dh\nu} F(h\nu) \frac{h\nu'}{h\nu} (1 - e^{-\sigma_P(h\nu')X_D}) dh\nu \quad (6)$$

which is to be compared with the direct signal:

$$S_D = \int_0^{\infty} \frac{dE}{dh\nu} e^{-\sigma_T(h\nu)X} (1 - e^{-\sigma_P(h\nu)X_D}) dh\nu \quad (7)$$

The 2 inch thick detectors have an extended response at high energies whereas $F(h\nu) (h\nu'/h\nu)$ has a maximum not too far above the K-edge of lead. Thus, the worst case will tend to occur for a low temperature $dE/dh\nu$. With this in mind, we calculate (6) and (7) for the particular case of a 2 inch thick by 2 inch diameter NaI detector filtered with

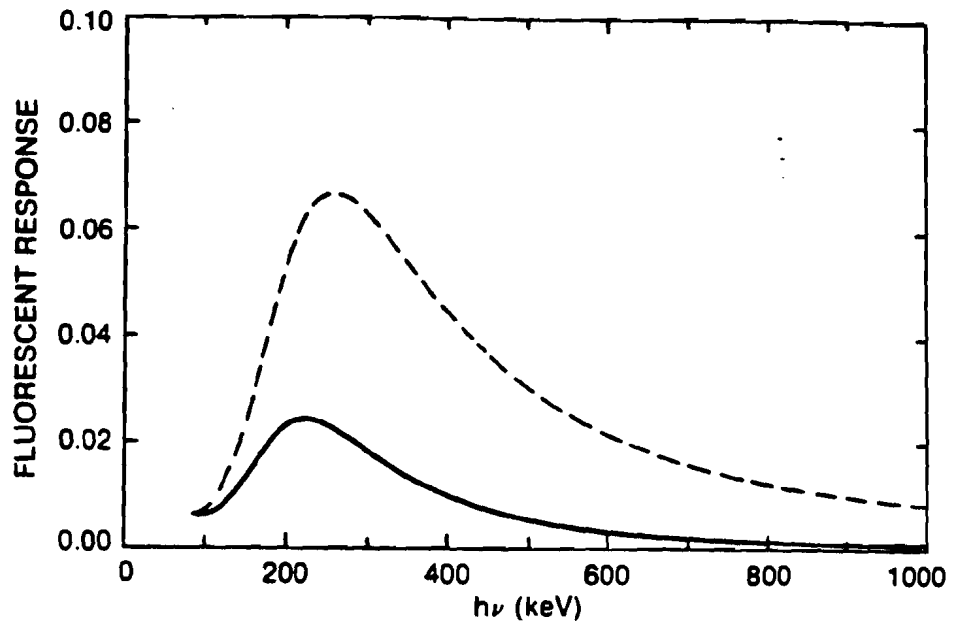


Figure D-2. Sensitivity of an NaI detector to foil fluorescence. Dashed curve shows number of photons detected, while solid curve shows energy transfer.

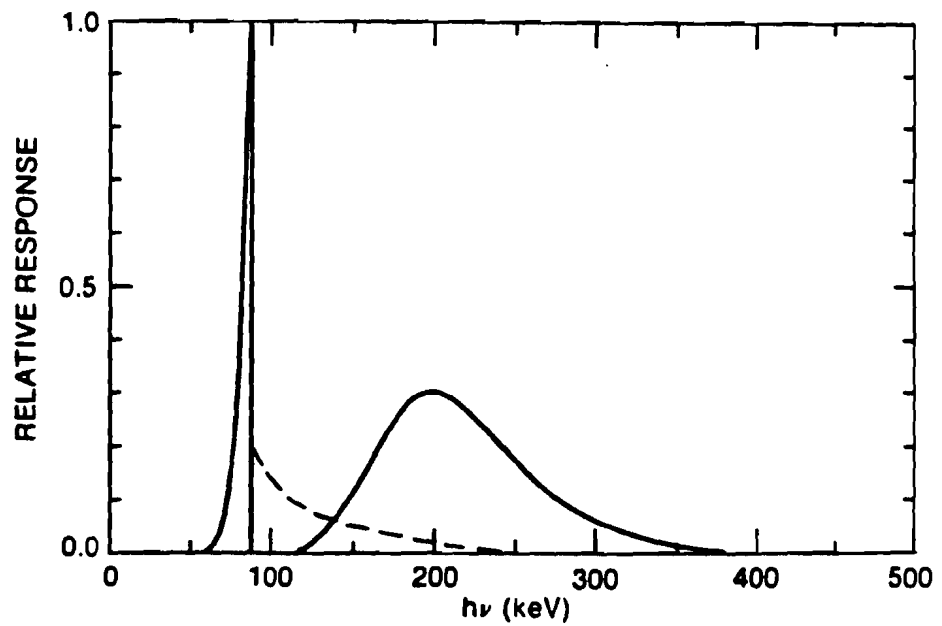


Figure D-3. Direct (solid curve) and fluorescent (dashed curve) signal obtained with a 30 keV incident x-ray spectrum.

2.54 mm of lead located 1 inch in front of the detector. $dE/dh\nu$ is a single 30 keV Maxwellian spectrum. The integrands of (6) and (7) are shown in figure D-3. The integrals are $S_F = 2.1 \times 10^{-3}$ and $S_D = 9.7 \times 10^{-3}$ so the fluorescence contributes about 20% of the signal. The values of S_F and S_D are shown in Table D-1 for several different conditions.

TABLE D-1. DIRECT AND FLUORESCENT DETECTOR SIGNAL

T (keV)	2.54 mm Pb		5.1 mm Pb	
	S_F	S_D	S_F	S_D
20	2.8E-04	6.9E-04	2.2E-06	1.7E-05
30	2.1E-03	9.7E-03	3.5E-05	9.4E-04
40	6.5E-03	5.8E-02	1.9E-04	9.4E-03
50	1.4E-02	2.0E-01	6.3E-04	4.2E-02

APPENDIX E
FILTER AND DETECTOR SELECTION CONSIDERATIONS

Our initial measurements with K-edge filtered detectors provided less than reliable results. This was caused by a number of factors which included improper filter thickness selection, insufficient energy range coverage and not enough detectors. The following guidelines for filter and detector selection are based on this experience.

A. FILTER THICKNESS SELECTION

Because detectors are available in limited types and configurations, the filter thickness is often the only parameter affecting the performance of a given K-edge detector over which there is any control. Figure E-1 illustrates how a detector system response varies with filter thickness. The detector utilized in this example is a 125 μm Silicon PIN diode and the filter is Iron.

The optimum filter thickness in this example is .025 mm. If the filter thickness is doubled to .050 mm, the response beyond the K-edge increases relative to the

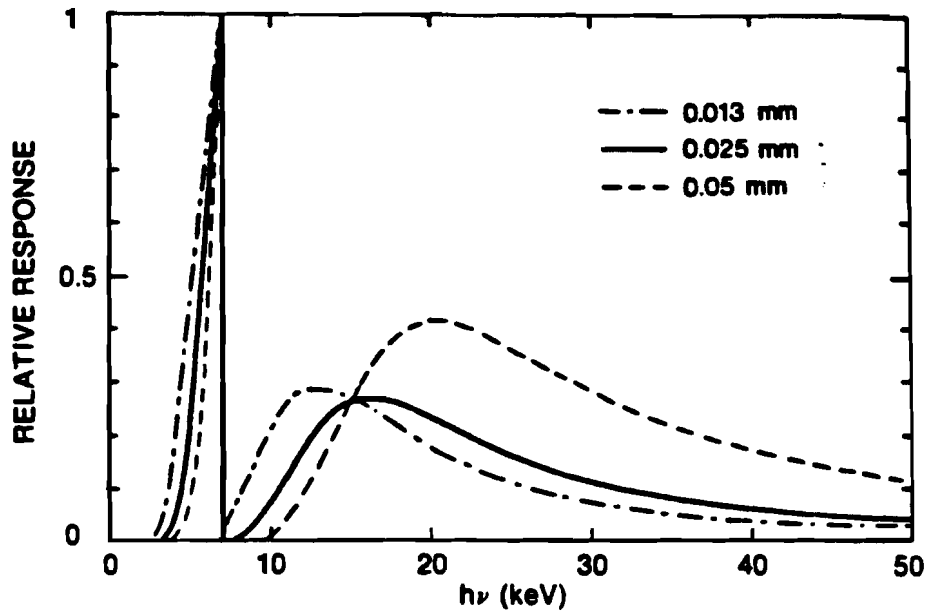


Figure E-1. Response obtained from Iron filtered PIN diode for several filter thicknesses.

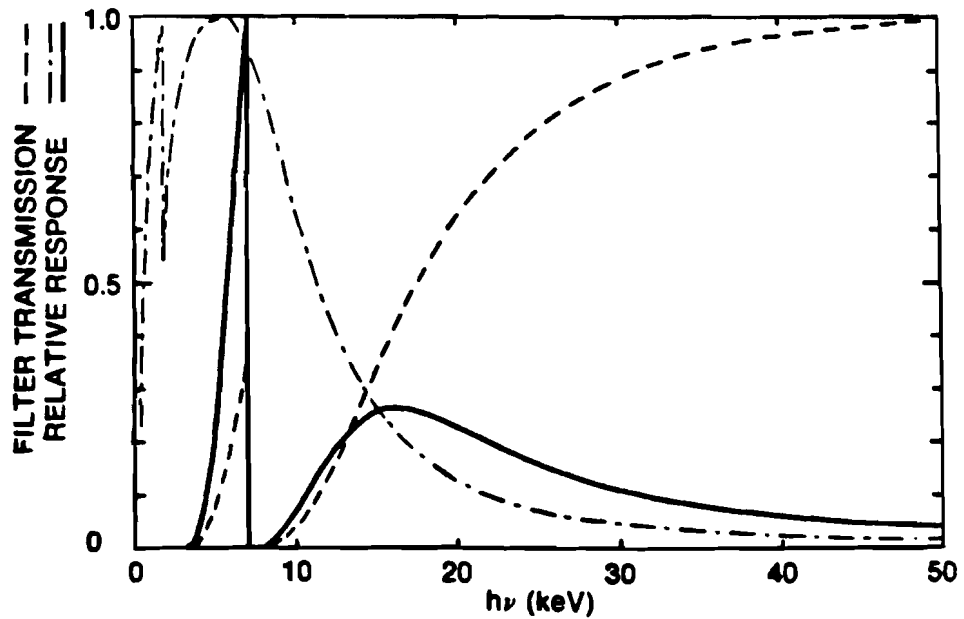


Figure E-2. Factors affecting detector performance (solid curve). Filter transmission (dashed curve) and detector sensitivity (dot-dashed curve).

response just below the K-edge. Thus a broad response at an energy considerably higher than the desired energy is obtained. If the filter thickness is decreased to .0125 mm, it will be seen that the response beyond the K-edge is very similar to that obtained at .025 mm. In addition the response below the K-edge has broadened with respect to that obtained at .025 mm. Thus, .025 mm would be the preferred thickness.

Choosing the filter thickness by plotting the response for several different filter thicknesses is quite useful, since it provides a feeling for the kind of compromises that can be made. As a guide however, the jump in response across the K-edge should be about a factor of 1000. Having selected a filter thickness, the spectrally weighted response should be plotted for spectra similar to those to be measured, since it may be desirable to alter the filter thickness slightly to accommodate a particular case. If this is done, trial spectra considerably different from expected should also be tested to ensure that reasonable performance is still obtained.

Because the exponential nature of the x-ray continuum results in a rapid decrease in detector signal level as the K-edge energy increases, there is a temptation to make the filters in low energy channels too thick in order to reduce the signal level and avoid detector saturation. This should

not be done, since as shown above, an overly thick filter results only in a broad response above the K-edge. If saturated detectors are a problem, the signal should be reduced either by aperturing the detectors or moving the detectors further from the source.

B. DETECTOR SELECTION

The response of a K-edge detector is determined by the product of the detector responsivity and the filter transmission. Referring to figure E-2, it can be seen that because the transmission of the filter increases to 100% well beyond its K-edge energy, the response of the K-edge filtered detector system at energies above the K-edge is limited by the fact that the detector sensitivity is decreasing in this region.

The figure illustrates a nearly ideal case: the K-edge transmission peak of the filter is located nearly at the peak in sensitivity of the detector and the the detector sensitivity is decreasing above the K-edge. The detector illustrated would clearly be less than optimal for filters with K-edges less than about 5 keV.

As has been noted, detector parameters are not totally under the experimentalist's control. To the extent possible however, the K-edge of the detector material should be

located below the K-edge of the filter being used and the detector thickness should be sufficient to place the K-edge of the filter just slightly beyond detector peak response.

C. K-EDGE ENERGIES

The selection of K-edge energies will depend somewhat on the method used to unfold the spectrum from the data. For the multi-Maxwellian method used in these experiments it was found that in so far as possible it is desirable to space the edges equally from T to about $10T$ in energy. With several T 's present, this should be done for each component. Compromises frequently have to be made, since foils with K-edges exactly where required are not usually available.

A related consideration is the number of detectors to use. Each exponential spectral component requires two parameters, T and N , to fit it. Hence, at least two detectors are required to determine each component. In our experience at least twice that number are required to obtain reliable results.

APPENDIX F
SCALING IN A NON-UNIFORM BEAM

The non-uniform nature of the 0.35 μm GDL beam can potentially result in a distortion of measured scaling of intensity dependent quantities particularly if they are measured near a threshold. This can be illustrated with a simplified example, where the beam is approximated with a gaussian radial profile. In fact the beam is nowhere near gaussian, but the measured beam intensity distribution dE/dI is reasonably approximated by the dE/dI for a gaussian beam and this is all that is important.

Consider a quantity T which scales as $I^{1/3}$. The signal from which T is determined is assumed to vanish below a threshold intensity I_T and to be proportional to the energy at intensities above I_T . In a non-uniform beam then the measured T , $\langle T \rangle$, will be the energy weighted average of $I^{1/3}$ over all areas of the beam above threshold:

$$\langle T \rangle \propto \frac{\int_{I > I_T} I^{1/3} dE}{\int_{I > I_T} dE}$$

$$\propto \frac{\int_{I_T}^{\infty} I^{1/3} \frac{dE}{dI} dI}{\int_{I_T}^{\infty} \frac{dE}{dI} dI}$$

For a gaussian radial beam profile, dE/dI is a constant for $I < I_0$, where I_0 is the peak beam intensity, and 0 for $I > I_0$, hence:

$$\begin{aligned} \langle T \rangle &\propto \frac{\int_{I_0}^{I_T} I^{1/3} dI}{\int_{I_0}^{I_0} dI} \\ &\propto \frac{I_0^{4/3} - I_T^{4/3}}{I_0 - I_T} \end{aligned}$$

Defining $\alpha \equiv I_0/I_T$:

$$\propto \frac{\alpha^{4/3} - 1}{\alpha - 1}$$

Then if T is measured at $\alpha = 1.5, 3$ and 6 , the measured scaling will be found to be $T \propto I_0^{0.23}$.

The value 0.23 is of course a function of the actual dE/dI of the beam and the detailed behavior of the signal near threshold. In addition it will depend on how close to threshold the measurements are made; for large α , the original $I^{1/3}$ scaling is obtained. In these experiments, measurements of T_{SH} scaling are generally being determined close to threshold. Thus on the GDL system, it is to be

expected that the measured scaling of T_{SH} is lower than the actual scaling of T_{SH} with intensity.

REFERENCES

1. R.S. Craxton, "Theory of high efficiency third harmonic generation of high power Nd-glass laser radiation", *Optics Comm.* 34, 474 (1980).
2. W. Seka, S.D. Jacobs, J.E. Rizzo, R. Boni, and R.S. Craxton, "Demonstration of high efficiency third harmonic conversion of high power Nd-glass laser radiation", *Optics Comm.* 34, 469 (1980).
3. W. Seka, R.S. Craxton, J. Delettrez, L. Goldman, R. Keck, R.L. McCrory, D. Shvarts, J.M. Soures, and R. Boni, "Measurements and interpretation of the absorption of 0.35 μ m laser radiation on planar targets", *Optics Comm.* 40, 437 (1982).
4. A.B. Langdon, B.F. Lasinski, and W.L. Kruer, "Nonlinear saturation and recurrence of the two-plasmon decay instability", *Phys. Rev. Lett.* 43, 133 (1979).
5. K. Estabrook, W.L. Kruer, and B.F. Lasinski, "Heating by Raman backscatter and forward scatter", *Phys. Rev. Lett.* 45, 1399 (1980).
6. K. Tanaka, L.M. Goldman, W. Seka, M.C. Richardson, J.M. Soures, and E.A. Williams, "Stimulated Raman scattering from UV-laser-produced plasmas", *Phys. Rev. Lett.* 48, 1179 (1982).
7. K. Tanaka, and L.M. Goldman, "Observations of Brillouin sidescatter in laser-produced plasmas", *Phys. Rev. Lett.* 45, 1558 (1980).
8. D.W. Phillion, D.L. Banner, E.M. Campbell, R.E. Turner, and K.G. Estabrook, "Stimulated Raman scattering in large plasmas", *Phys. Fluids* 25, 1434 (1982).
9. D.W. Phillion, E.M. Campbell, K.G. Estabrook, G.E. Phillips, and F. Ze, "High-energy electron production by the Raman and 2ω instabilities in a 1.064- μ m-laser-produced underdense plasma", *Phys. Rev. Lett.* 49, 1405 (1982).
10. R.G. Berger, R.D. Brooks, and Z.A. Pietrzyk, "Observation of suprathreshold electrons produced by stimulated Raman scattering processes", *Phys. Fluids* 26, 354 (1983).
11. N.A. Ebrahim, H.A. Baldis, C. Joshi, and R. Benesch, "Hot electron generation by the two-plasmon decay

- instability in the laser-plasma interaction at $10.6 \mu\text{m}$ ", Phys. Rev. Lett. 45, 1179 (1980).
12. J.H. McAdoo, "Super Hard X-Rays From Two-Plasmon Decay In Laser Produced Plasmas", Ph.D. Thesis 1981, University of Rochester, Mechanical Engineering Department.
 13. K.R. Manes, H.G. Ahlstrom, R.A. Haas, and J.F. Holzrichter, "Light-plasma interaction studies with high-power glass laser", J. Opt. Soc. Am. 67, 717 (1977).
 14. D.C. Slater, Gar. E. Busch, G. Charatis, R.R. Johnson, F.J. Mayer, R.J. Schroder, J.D. Simpson, D. Sulliman, J.A. Tarvin, and C.E. Thomas, "Absorption and hot-electron production for 1.05 and $0.53 \mu\text{m}$ light on spherical targets", Phys. Rev. Lett. 46, 1199 (1981).
 15. K.G. Estabrook, E.J. Valeo, and W.L. Kruer, "Two-dimensional relativistic simulations of resonance absorption", Phys. Fluids 18, 1151 (1975).
 16. D.W. Forslund, J.M. Kindel, and K. Lee, "Theory of Hot-Electron Spectra at High Laser Intensity", Phys. Rev. Lett. 39, 284 (1977).
 17. K. Estabrook, and W.L. Kruer, "Properties of Resonantly Heated Electron Distributions", Phys. Rev. Lett. 40, 42 (1978).
 18. A. Simon, R.W. Short, E.A. Williams, and T. Dewandre, "On the Inhomogeneous Two Plasmon Instability", (to be published).
 19. C.S. Liu, and M.N. Rosenbluth, "Parametric decay of electromagnetic waves into two plasmons and its consequences", Phys. Fluids 19, 967 (1976).
 20. B.F. Lasinski, A.B. Langdon, K.G. Estabrook, and W.L. Kruer, "Heating and Hot-Electron Generation in Underdense Plasmas", 1980 Annual Report UCRL-50021-80, 3-30 (1981).
 21. K.A. Brueckner, "Fast-electron production in laser-heated plasmas", Nuclear Fusion 17, 1257 (1977).
 22. K.G. Tirsell, "Multichannel Filter-Fluorescer Experiment for X-Ray Spectral Measurements above 2 keV", Laser Program Annual Report-1977 UCRL-50021-77 3-64 (1978).
 23. W.J. Veigele, "Photon Cross Sections from 0.1 KeV to 1

- MeV for elements $Z = 1$ to 94", Atomic Data 5 (1973) pp. 51-111.
24. W.H. McMaster, N. Kerr Del Grande, J.H. Mallet, J.H. Hubbell, "Compilation of X-ray Cross Sections", National Technical Information Service UCRL-50174-SEC 2-R1 (1969).
 25. C.M. Davisson, "Interaction of α -Radiation with Matter", in Alpha-, Beta- and Gamma-Ray Spectroscopy, Kai Siegbahn, ed., (North-Holland: Amsterdam, 1974) p. 50.
 26. Ibid., pp. 38-39.
 27. D.M. Corallo, D.M. Creek, and G.M. Murray, "The x-ray calibration of silicon p-i-n diodes between 1.5 and 17.4 keV", J. Phys. E: Sci. Instrum. 13, 623 (1980).
 28. Harshaw Scintillation Phosphors, (Harshaw Chemical Co.: Solon, Ohio, 1969).
 29. Kenro Miyamoto, Plasma Physics for Nuclear Fusion, (MIT Press: Cambridge, Mass., 1980) p. 478.
 30. IMSL documentation.
 31. N.R. Draper, and H. Smith, Applied Regression Analysis, (John Wiley & Sons: New York, 1981).
 32. W. Seka, J.M. Soures, S.D. Jacobs, L.D. Lund, and R.S. Craxton, "GDL: A high-power 0.35 μm laser irradiation facility", IEEE J. Quantum Electron. QE-17, 1689 (1981).
 33. J. Bunkenberg, J. Boles, D.C. Brown, J. Eastman, J. Hoose, R. Hopkins, L. Iwan, S.D. Jacobs, J.H. Kelly, S. Kumpan, S. Letzring, D. Lonobile, L.D. Lund, G. Mourou, S. Reformat, W. Seka, J.M. Soures, and K. Walsh, "The Omega high-power phosphate-glass system: design and performance", IEEE J. Quantum Electron. QE-17, 1620 (1981).
 34. M.C. Richardson, (personal communication).
 35. R.S. Craxton, (personal communication).
 36. W. Seka, (personal communication).
 37. B. Yaakobi, J. Delettrez, L.M. Goldman, R.L. McCrory, W. Seka, and J.M. Soures, "Preheat measurements in UV-laser target interaction", Optics Comm. 41, 355 (1982).

38. Ralph W. Engstrom, Photomultiplier Handbook, (RCA: Lancaster, PA, 1980) p. 45.